Journal of the Meteorological Society of Japan

EARLY ONLINE RELEASE

The DOI for this manuscript is
DOI:10.2151/jmsj.2022-016
J-STAGE Advance published date: December 10th, 2021
The final manuscript after publication will replace the preliminary version at the above DOI once it is available.

Bias in Near-Real-Time Global Sea Surface Temperature Analysis of Japan Meteorological Agency Associated with Tropical Cyclone Passages in Western North Pacific

Kosuke ITO

University of the Ryukyus, Nishihara, Japan

Meteorological Research Institute, Tsukuba, Japan

Accepted to *Journal of the Meteorological Society of Japan*

November, 2021

----

1) Corresponding author: Kosuke Ito, *University of the Ryukyus, Nishihara, Japan*

Meteorological Research Institute, Tsukuba, Japan

Email: itokosk@sci.u-ryukyu.ac.jp

Tel: +81-98-895-8573

Fax: +81-98-895-8552

Abstract

The near-real-time merged satellite and *in-situ* data global daily sea surface temperature (SST) of the Japan Meteorological Agency (hereinafter abbreviated as R-MGD) is subjected to filtering out short-time-scale fluctuations from the observations prior to the analysis time. Therefore, the rapid SST change due to the passage of tropical cyclones (TCs) is thought to cause biases. Here the biases in the R-MGD, with respect to *in-situ* observations, were quantified along the passage of TCs in the western North Pacific. First, we examined a case study on the approach of three successive TCs in August–September 2020. The R-MGD had positive biases of >2℃ just after the passage of three TCs, while negative biases were observed after one week of the last TC's passage. The comparison of the R-MGD with a moored buoy indicates that the biases can be explained by short-term fluctuations filtered out and the SST prior to the analysis time in the R-MGD analysis. Second, the composite analysis from May 2015–October 2020 indicates that the statistically significant biases at the observation points ranged between -1 day and +4 days for positive biases and between +7 days and +14 days for negative biases relative to the time of the closest approach of a TC within 500 km. The positive SST bias is largely associated with cold subsurface water and intense TCs, being pronounced in the mid-latitude except around the Kuroshio and the Kuroshio extension regions. The assimilation of *in-situ* observations recorded within 72 h prior to the R-MGD analysis time through additional optimal interpolation alleviates these biases because

this process redeems short-time-scale fluctuations. The impact on TC forecasts and the validity of the optimal interpolation experiment against the independent observations were also investigated.

Keywords: sea surface temperature; tropical cyclones; optimal interpolation; western North Pacific; Japan Meteorological Agency

1. Introduction

The quality of near-real-time daily sea surface temperature (SST) analysis is important for weather prediction, oceanic prediction, oceanic ecosystems, and fishery activities. In terms of disaster prevention and mitigation, the improvement of near-real-time SST analysis can contribute to enhancing weather forecasting because severe weather events such as heavy rainfall events and tropical cyclones (TCs) are sensitive to SST (Emanuel 1986; Iizuka and Nakamura 2019; Ito and Ichikawa 2021; Kusunoki and Mizuta 2008; Manda et al. 2014; Moteki and Manda 2013; Nayak and Takemi 2019; Tsuguti and Kato 2014).

Currently, the Japan Meteorological Agency (JMA) creates several SST analysis products. Daily SSTs in the global ocean are objectively analyzed in a near-real-time and delayed-mode, called the merged satellite and *in-situ* data Global Daily Sea Surface Temperature (MGDSST; JMA 2019; Kurihara et al. 2006). Meanwhile, the JMA has also conducted another SST analysis for climate monitoring known as COBE-SST (Ishii et al. 2005), along with High-resolution merged satellite and *in-situ* data Sea Surface Temperature (HIMSST; https://ds.data.jma.go.jp/gmd/goos/data/pub/JMA-product/him_sst_pac_D/Readme_him_sst_pac_D). Among MGDSST, COBE-SST, and HIMSST, the near-real-time version of MGDSST (referred to as R-MGD in this study) uses preprocessed satellite and *in-situ* observations from 17 days before the analysis time. R-MGD has been used as the boundary condition for simulations, with an atmospheric global spectral model (GSM) and also as the “observations” that are assimilated in the ocean data assimilation system used for the global model and North Pacific model (Hirose et al. 2019; JMA 2021; Sakamoto et al. 2019). Although the boundary condition of the operational mesoscale model has been HIMSST since March 2019 (https://www.jma.go.jp/jma/kishou/books/nwptext/52/No52_all.pdf), R-MGD can indirectly influence their skills through the lateral boundary condition. Therefore, R-MGD is very important for weather and ocean predictions and ocean monitoring as the near-real-time information. While the R-MGD utilizes the observations available prior to the analysis time, JMA also performed the delayed-mode analysis of MGDSST (referred to as D-MGD in this study) by utilizing observations within 10 days before and after the analysis time. D-MGD is not available for weather and ocean forecasts, however, it provides more reliable SST field for research purposes and climate studies.

The procedure for generating the R-MGD carried out by JMA (as of December 11, 2020) is briefly summarized in Fig. 1 (Kurihara et al. 2006; personal communication, JMA Office of Marine Prediction). Firstly, the quality control and preprocessing are applied. For example, it has been known that SSTs obtained from the Advanced Very High Resolution Radiometer have systematic biases due to aerosols and clouds (Huang et al. 2015; Zhang et al. 2004). The biases are adjusted based on the match-up to the statistics of buoys. After quality control and preprocessing, five types of Gaussian filtering in space and time are applied to the SST anomaly data (with respect to the climatology) obtained from satellite infrared sensors and microwave sensors having weight w. The weight is determined using the following equation:

$$w = \frac{1}{(2\pi)^{3/2}\sigma_x\sigma_y\sigma_t}\exp\left(-\frac{1}{2}\left\{\frac{d_x^2}{\sigma_x^2}+\frac{d_y^2}{\sigma_y^2}+\frac{d_t^2}{\sigma_t^2}\right\}\right) \tag{1}$$

Here, σ_x and σ_y are the zonal and meridional filtering scales in km, respectively, and σ_t is temporal filtering scale in day. Their weights become small by a factor of $e^{-1/2}$, while d_x (in km), d_y (in km), and d_t (in day) represent the corresponding distances between the analysis and observation points. As for the temporal filtering, two filters $\sigma_t = 27.0\sqrt{\log 2/2\pi^2} \approx 5.06$ days and $\sigma_t = 53.0\sqrt{\log 2/2\pi^2} \approx 9.93$ days are used. They are conventionally referred to as “27-day filter” and “53-day filter”, respectively, because the output power spectrum becomes halved for a sufficiently long input dataset[1]. After Gaussian filtering, the long and large scale of the SST anomaly field was adjusted to the long and large scale of *in-situ* observations, as carried out by Reynolds and Smith (1994) and Reynolds et al. (2002). Finally, they were merged using optimal interpolation (OI) (Fig. 1).

The strategy of R-MGD analysis to use a time-filtered dataset for daily analysis is understandable considering the large inertia of the ocean and the insufficient amount of data.

---

[1] Using a Fourier transform, the ratio r between the input and output power spectrum is $r = \exp\left(-2\pi^2\left(\sigma_x^2/\lambda_x^2+\sigma_y^2/\lambda_y^2+\sigma_t^2/T^2\right)\right)$. Thus, the output power spectrum were halved of the input, $r = 1/2$, in the time scale of T = 27.0 days for $\sigma_t \approx 5.06$ days and T = 53.0 days for $\sigma_t \approx 9.93$ day if the dataset were sufficiently long in time. In fact, the output power spectrum is more than half for 27 days and 53 days because the data length is not sufficient. Although the terms “27-day filter” and “53-day filter” are inappropriate in this sense, we use these terms following the convention. The same notion is applied to spatial filtering.

If we do not apply temporal filtering nor prepare a background field, it is difficult to avoid unphysical SST structures, such as sharp changes and missing values. Nevertheless, it should be noted that the actual rapid SST changes in the last few days are substantially dropped from the R-MGD because of the rather long-time-scale temporal filtering. Such an example is SST cooling and SST recovery occurring in a short-time scale caused by the passages of TCs (Dare and McBride 2011; Price et al. 2008).

In general, SST is affected by the air-sea fluxes including radiation, entrainment, and detrainment of water at the base of the ocean mixed layer (OML) through vertical mixing, vertical transport, and horizontal transport. Commonly, while solar heating at daytime warms and stabilizes the upper ocean, winds enhance the ocean turbulence that mixes the water vertically and wind-induced circulation also plays an important role on the SST distribution (Price et al. 1986). As for the passage of TCs, winds can cause the SST to decrease mainly because of the one-dimensional vertical mixing and three-dimensional upwelling processes (Price 1981; Shay 2010; Yablonsky and Ginis 2009). The one-dimensional vertical mixing process is related to the storm-induced current in the OML. The difference of horizontal currents serving as a vertical shear becomes strong across the base of the OML, satisfying the critical Richardson number; thus, the cold water underneath is entrained into the OML. The OML increases in thickness and the waters become colder. This process is pronounced on the right-rear side of the TC center position, primarily because the wind stress vector turns clockwise in resonance with the near-inertial motion slightly enhanced by the asymmetric distribution of wind field (Price 1981). Thus, the region of large SST decrease is basically parallel to the TC motion. In addition to this vertical one-dimensional process, cyclonic wind forcing transports the upper ocean water horizontally away from the TC center. This surface transport induces an upwelling near the TC center. As a result, cold water is transported to the upper ocean in a three-dimensional manner. While vertical mixing is generally a primary mechanism in SST cooling, a strong upwelling becomes dominant for a very slow-moving cyclone (Kanada et al. 2021; Yablonsky and Ginis 2009). After the passage of TCs, the re-stratification of the upper ocean requires approximately one month, in which a rapid SST increase is seen in the first two weeks, as examined by Mei and Pasquero (2012); their study suggested that the increasing net radiation inputs speed up the SST recovery, in which the baroclinic instability plays an important role in the structure of the ocean temperature. The composite analysis of the SST from Argo data in the western North Pacific shows that the SST decrease starts one day prior to the passage of a TC (Wu and Chen 2012) and that three-quarters of SST decrease recover in 15 days (Lin et al. 2017).

Both the one-dimensional and three-dimensional SST cooling processes are relevant to the time scale of the inverse of the Coriolis parameter, f^{-1}, and the SST increases in several weeks during the recovery process. Because the temporal filtering in the R-MGD and D-MGD analyses overlooks the short-term SST changes, a part of the actual SST change can be discarded. In particular, the R-MGD only reflects the observed SSTs in the past with respect to the analysis time. When a high SST dropped in a short-timescale, the

R-MGD partly inherits the high SST according to the weight in Eq. (1) (Fig. 2a). The positive SST biases are expected to be large when the SST decrease is large, with cold water present just below the sea surface and the occurrence of strong and slow-moving TCs. The negative SST biases in R-MGD may appear also during the SST recovery stage if the SST increase is rather fast (Fig. 2b).

Therefore, the first aim of this work is to describe the SST biases in the R-MGD with respect to the TC passage based on a case study and composite analysis. The second aim is to propose a method for alleviating these biases by utilizing the *in-situ* observations obtained just before the SST analysis time. The remainder of this paper is organized as follows. In Section 2, we explain the data and methodology used for the study. Section 3 exemplifies the SST biases in the R-MGD caused by the passage of three TCs during August–September 2020. Composite analysis of the SST biases in the R-MGD for the period of May 2015–October 2020 is presented in Section 4. This section also reveals the physical background of the SST biases. In Section 5, we demonstrate that the additional OI of the *in-situ* observations (within 72 h prior to the R-MGD analysis time) can alleviate the SST biases. In Section 6, we conducted numerical experiments with the JMA non-hydrostatic model (JMA-NHM) to show the impact of updated SST on the TC forecasts. In Section 7, we discuss the validity of the OI experiment against the independent observations. Finally, our conclusions are summarized in Section 8. Additional results for the other basins and products are described in Supplements 1–6. For example, the negative and positive SST biases are respectively expected in D-MGD before and after the analysis time (Fig. 2c-d), and Supplement 1 describes the biases of D-MGD.

2. Data and method

The successive passages of TCs, Bavi, Maysak, and Haishen, during August–September 2020 were used as a case study to exemplify the biases in the R-MGD. The composite analysis from May 2015 to October 2020 (66 months) within the target region of 100°E–180° and 0°–60°N, was performed (detailed in Section 4), which corresponds to the region responsible for the Regional Specialized Meteorological Center Tokyo (RSMC Tokyo). In this paper, we focus on the western North Pacific because the analysis of tropical cyclone intensity and genesis is conducted by a different agency in each basin and because JMA high-quality daily ocean temperature is available during this period for the western North Pacific. We briefly discuss the global SST biases caused by TC passages in Supplement 2.

The R-MGD is the daily SST dataset of the global ocean on a grid of 0.25° × 0.25° every day (JMA 2019; Kurihara et al. 2006). The preprocessed SST data obtained from each satellite infrared or microwave sensor were subjected to five types of filters (Fig. 1), while the long and large-scale filtered component was adjusted by *in-situ* SST observations. The data from each filter and each satellite were finally merged through OI. The R-MGD at day *m* refers to the value averaged from 1800 UTC on day *m*-1 through 1800 UTC on day *m* (personal communication, JMA). Note that weather forecasts based on JMA's GSM (also referred to as JMA-GSM), with an initial time of 1800 UTC on day *m* and 0000 UTC, 0600 UTC, and 1200 UTC on day *m*+1 employs the R-MGD on day *m*. We also used the D-MGD in later sections. The climatological mean SST refers to the mean value of D-MGD between 1984 and 2014. Currently, the D-MGD is available only until December 2019.

In-situ observations were taken from *in-situ* SST Quality monitoring (*i*Quam) developed at NOAA (Xu and Ignatov 2014) (available at https://www.star.nesdis.noaa.gov/socd/sst/iquam/data.html; accessed on November 19, 2020). The *i*Quam is a globally compiled *in-situ* SST dataset obtained from ships, drifters, moored buoys, and Argo floats having a quality control (QC) flag. The QC processes comprised preprocessing (resolving duplicates from multiple transmission or dataset merging), plausibility/geolocation, internal consistency, external consistency, and mutual consistency checks. Based on these tests, a quality flag is appended to each observation (Table 7 of Xu and Ignatov (2014)). For reliability, we used only the data with the QC flag of "best quality" and did not use the data having "acceptable quality" and "low quality" unless otherwise noted. Note that neglecting the "acceptable quality" and "low quality" data may lead to some underestimation of the SST biases, as we shall see in Fig. 8 and Supplement 3. We used only one randomly sampled data of the day from one platform for the composite analysis in Section 4 when two or more data were available.

The TC center position and intensity were taken from the best track of RSMC Tokyo (https://www.jma.go.jp/jma/jmaeng/jma-center/rsmc-hp-pub-eg/besttrack.html). The best track data is not considered before a TC reaches the threshold of tropical storm status or an extratropical cyclone subjected to transition from the TC. TC translation speed was simply calculated from the difference in the TC's center positions in the next 6 h. Fig. 3 shows the 6-hourly center positions of 153 TCs used for the composite analysis.

We stratified the data according to the difference of pre-storm ocean temperature between 50 m and 1 m (δT_{50}), TC maximum wind speed, and TC translation speed. The oceanic data is given by the JMA-Meteorological Research Institute (MRI) Multivariate Ocean Variational Estimation system (MOVE; JMA 2019; Usui et al. 2006; Usui et al. 2017), in which the base physical model is the MRI Community Ocean Model (Tsujino et al. 2017). Since a high-resolution four-dimensional variational data assimilation system did not cover the entire target region for the period of interest, we used daily outputs having a horizontal grid spacing of 0.5° obtained from a three-dimensional variational data assimilation system for the North Pacific Ocean. Note that the R-MGD was assimilated into the operational ocean model as the "observations" into the MOVE system. Large negative values of δT_{50} represent very cold water at 50 m relative to the surface water. We also used the satellite-based SST from the Global Change Observation Mission 1st-Water (GCOM-W1) Advanced Microwave Scanning Radiometer 2 (AMSR2) onboard the GCOM-W1 satellite. It is a remote sensing instrument for measuring microwave emission from the surface. Here, we employed the L3 standard product which has the horizontal grid spacing of 0.25° (available at https://gportal.jaxa.jp/gpr/?lang=en).

The gridded analysis data are linearly interpolated in space to compare them with *in-situ* observations. As for temporal interpolation, we simply calculated the difference between an *in-situ* observation from 1800 UTC on day m-1 to 1800 UTC on day m and the corresponding R-MGD on day m. For presentation purposes, we refer 1800 UTC at day m as the R-MGD analysis time. While the daily mean of the MOVE refers to the value averaged from 0000 UTC on day m through 0000 UTC on day m+1, the influence of the time lag of 6 h was at most 0.1℃ in terms of the composite mean SST bias and was thus negligible.

We categorized the SST bias data according to the relative time and location with respect to the TCs. This was achieved by employing the TC's closest approach distance to an *in-situ* observation, d_m, and the observation time relative to the time of the closest approach, $\Delta t = t_{obs}-t_{bst}$ (Fig. 4). For a given observation at the observed time t_{obs}, we first seek the TC center position at the time t_{bst} that exhibited the closest approach within 1000 km from the observation point, while satisfying $-5 < \Delta t < +15$ days. According to the previous studies, the TC-induced SST cooling starts from one day prior to the TC passage and three-quarters of the SST cooling are recovered in 15 days after the TC passage (Lin et al. 2017). Therefore, the period of $-5 < \Delta t < +15$ days is sufficient to quantify SST biases in a background, rapidly decreasing, and rapidly increasing stages. Although weak TC-induced SST anomalies may persist for more than 15 days (Lin et al. 2017; Mei and Pasquero 2012), we did not analyze the data beyond 15 days because it is too long to elucidate the influence of the TC. As for the relative position of an observation, the positive d_m is defined as the closest approach distance when the observation is on the right-hand side of the direction of the TC motion, while the negative d_m indicates the observation on the left-hand side. Note that d_m almost corresponds to the cross-track distance (perpendicular to the TC motion direction) from the observation point to the TC's closest approach point, as shown in Fig. 4. It reveals when the SST bias appears and how long it persists after the TC's closest approach. If the TC center position was not recorded within 1000 km from the observation point during the target period, the observation was not used in the composite analysis. If more than one TC approached the observation point, only the TC with the smallest $|d_m|$ was analyzed. The total number of available *in-situ* observations with the best-quality flag is approximately 9.1×10^6 from May 2015 to October 2020 in 100°E–180° and 0°–60°N. Sampling only one data point from the same platform on one day yielded 5.7×10^5 observations (Fig. 5a), we used 1.4×10^5 observations for the composite analysis to evaluate the influence of the TC passages (Fig. 5b). In addition to the coordinates spanned by d_m and Δt, we also used a so-called TC centered coordinate that looks down the direction of the TC motion as an ordinate axis, while the TC center position is located at the origin of the coordinate. In this coordinate, the abscissa and ordinate axes correspond to the cross-track and along-track distances, respectively.

In fact, the mean biases discussed in the later sections are slightly different between the ships and the other observation platforms by about 0.05-0.10 K (average: 0.07 K) within $|d_m| < 500$ km as consistent with the statistics of Xu and Ignatov (2014). We basically neglect this difference because it is much smaller than the TC-induced biases. We are not sure about the reason for this, but it can result from a ship-based observation deployed in a shallow level on average[2] or the influence of the engine of a ship.

3. Case study in August–September 2020

From August 23, 2020 to September 7, 2020, TCs Bavi, Maysak, and Haishen successively passed around the East China Sea, Yellow Sea, and Japan Sea. According to the RSMC Tokyo best track, the lifetime maximum wind speed of these TCs were 85 kt, 95 kt, and 105 kt, respectively. All TCs exhibited the maximum wind speed of 85 kt or more over the East China Sea or Yellow Sea. Here, we exemplify the SST biases in the R-MGD along the passage of these TCs. Fig. 6 shows that the SSTs were over 30℃ in the eastern part of the East China Sea, which was much higher than the climatological SST during the pre-storm period on August 20. At that moment, the SST biases in the R-MGD were relatively small, except for some negative biases along the east and south coast of the Korean Peninsula (Fig. 6a). The SST biases tended to become positive around +1℃ along the track of Bavi (Fig. 6b). On August 29–31, the positive SST bias reached +2–3℃ after a few days in the Yellow Sea in a wake of Bavi and +0.5℃ to the east of the Philippines around the center of TC Maysak (Fig. 6c). It is also notable that a negative SST bias appears along the

[2] We cannot evaluate the influence of observation depths because they are not recorded for ship-based observations in *i*Quam.

track of Bavi in the south of East China Sea. Fig. 6d shows that the SST biases in R-MGD were around +2℃ in the East China Sea and Yellow Sea. The positive SST biases of more than 3℃ were also remarkable in the southwestern part of the Sea of Japan (Fig. 6d). Although the SSTs in R-MGD decreased by 2–4℃ in the Yellow Sea and East China Sea along the passages of TCs Bavi and Maysak in two weeks until September 4, the comparison with the *in-situ* data shows that the SST decrease in the R-MGD was still insufficient to represent the actual SST drop. On September 4, a positive SST bias in the right-rear of the track of TC Haishen was also observed. After Haishen's transition to the extratropical cyclone, negative biases less than -1.5℃ continued in existence for more than one week in the East China Sea, Yellow Sea, and western part of the Sea of Japan (Fig. 6e–f). To sum up the observations, the positive SST biases in the R-MGD emerged for several days along the TC track, while the negative SST biases appeared after about one week and continued for another week.

These characteristics of R-MGD were also seen in the SSTs from GCOM-W1 AMSR2. Fig. 7a and 7b show that the SST dramatically decreased according to the passage of three TCs. However, the magnitude of decrease is exceedingly weak in R-MGD, particularly, just after the passage of TC Haishen (Fig. 7b). AMSR2 SST indicates an increase of SST as a recovery after the passage of TCs such as in 134°E–145°E and 18°N–30°N (Fig. 7c). In contrast, R-MGD remains cold relative to AMSR2 SST.

We compared the R-MGD at 126.03°E and 33.08°N with the observations made by the coastal moored buoy ID 22107 at Marado operated by Korean Meteorological Agency (KMA), including the non-“best quality” ones (Fig. 8). The buoy-based SST substantially dropped from 30.1℃ to 24.5℃ in only four days (August 23–27); it decreased from 28.9℃ (August 25) to 25.4℃ (August 26) in one day. This is consistent with the passage of TC Bavi that approached this region on August 25–26. After the passage of Bavi, the buoy-based SST increased toward the climatological mean SST and became 26.3℃ on August 30. However, on the successive approaches of TCs Maysak and Haishen, the buoy-based SST decreased again and remained around 24℃ until September 8. After the passage of the three TCs, in the middle of September, the buoy-based SST increased toward the climatological mean SST.

In contrast to the rapid change in the moored buoy, the temporal change in R-MGD was exceedingly gentle. This led to a large overestimation of the SST in R-MGD on and just after the passage of the TCs. An SST bias of more than +1℃ was continually observed from August 25 to September 5; the maximum SST bias reached +4.8℃ on August 27. It is also notable that the restoration of the SST toward the climatological value (at the end of August and in the middle of September) was not seen in the R-MGD. This causes the negative SST bias to be approximately -1℃ in mid-September. In contrast, the SST bias was positive at the end of August, presumably because a very gentle decrease in the R-MGD was insufficient to catch up the dramatic decrease in the moored buoy. In addition, the passage of TC Maysak further decreased the SST at that moment. In fact, the dramatic decrease in the SST was obvious by the AMSR2 product at the nearest grid point. This implies that the SST biases in the R-MGD were well captured by, at least, some satellite observations, but the temporal filtering that uses the “27-day” scale or more and the availability of the data in the near-real-time prevent the rapid SST decrease in the R-MGD analysis. We also show the time-series in Operational Sea Surface Temperature and Sea Ice Analysis (OSTIA), which is the near-real-time version of SST analysis operationally conducted by United Kingdom Meteorological Office (Donlon et al. 2012). The bias in OSTIA is smaller than in R-MGD for the rapid SST decrease and increase. OSTIA is expected to better capture short-term SST changes because the main analysis process employs a previous analysis field as a first guess field and digests the observations within a 36-h assimilation window through an optimal interpolation approach (Donlon et al. 2012).

Fig. 9a shows the power spectrum of the SST anomaly (relative to the daily climatology) from July 2015 through June 2020 for this moored buoy. The power of high-frequency mode was largely suppressed in the R-MGD analysis as expected from the temporal smoothing. The power of the R-MGD is half for the period of <20 days and only one-tenth for the period of <5 days. It suggests that the TC-induced rapid SST change in a few days is hardly reproduced in the R-MGD analysis. In contrast, the power for the period of a few days was much stronger in GCOM-W1/AMSR2 than the moored buoy probably due to the nature of the polar orbital satellite that estimated the SST from snapshots. To ensure the characteristics of R-MGD, we investigated the SST change in the Kuroshio extension region. The suppression of high-frequency component was also seen in the moored buoy at Kuroshio Extension Observatory (KEO; 32.3°N and 144.6°E) (Fig. 9b). The power of the R-MGD is half for the period of <15 days and only one-tenth for the period of <8 days.

4. Composite analysis

Fig. 10a shows the composite bias of R-MGD with respect to the *in-situ* observations in a d_m-Δt coordinate for all the cases. The positive bias of the R-MGD in $-0.5 < \Delta t < 3.5$ days is statistically significant, with a confidence level of 95%, as found by using a two-sided *t*-test. The region of the statistically significant positive biases ranges around 500 km on each side. In other words, the positive SST bias, with a bandwidth of several hundred kilometers, persists for a few days along the TC path. The mean positive bias between $-150 < d_m < 250$ km in $-0.5 < \Delta t < 3.5$ days was +0.40℃. The maximum positive value of +0.52℃ was observed at $d_m = 0$ km and $\Delta t = 2$ day. The bias tended to be large at the center and on the right-hand side of the TC track. This presumably corresponds to the shear-induced SST decrease along the TC passage (Ito et al. 2015; Price 1981; Price et al. 1994). Another notable feature of Fig. 10a is that the negative SST bias peaked at the value of -0.29℃ in 7.5–13.5 days after the passage of the TCs. It represents that the restoration of the SST toward the climatological mean value was not captured in the R-MGD analysis, as exemplified at Marado in the mid-September of 2020 (Fig. 8). In terms of forecasts, a detrimental impact can last for at least a couple of weeks after the TC passage. In a TC centered coordinate, a statistically significant SST bias was found between 200 km ahead of the TC center and 700 km behind the TC center (Fig. 10b). We can ensure that the positive bias was larger at the center and on the right-hand side of the TC track.

According to previous studies (Lin et al. 2008; Yablonsky and Ginis 2009), the TC-induced SST decrease depends on the upper ocean thermal structure, TC intensity, and translation speed of the TC. Because large SST decreases are likely to incur a large SST bias in the R-MGD, we stratified the SST biases according to the deviation of ocean temperature at 50-m depth, with respect to the ocean temperature at 1 m, at Δt = -3 days both obtained from MOVE (δT_{50}), maximum wind speed at the closest approach (V_{max}), and TC translation speed at the closest approach (U). Fig. 11a–c show the composite mean of three groups stratified according to δT_{50}. The thresholds of each group were determined to approximately contain the same number of samples. The SST bias is much larger when the ocean temperature at 50 m is much cooler than the sea surface (Fig. 11a–c). This result is consistent with the fact that a large SST decrease is expected with cold water just beneath the surface. The positive bias reached up to +1.16℃ near the TC center three days behind the closest approach of a TC. The SST bias was also large when the maximum wind speed V_{max} was strong (Fig. 11d–f). It seems a little surprising that relatively large positive biases are associated with the fast-moving TCs (Fig. 11g–i) because slow-moving TCs generally induce a large SST decrease due to persistent wind (Lin et al. 2008; Price 1981; Yablonsky and Ginis 2009). This can be explained by the spurious correlation, as shown in Fig. 12.

Fig. 11 shows that the duration of positive biases and negative biases was not dependent on the classification according to δT_{50}, V_{max}, and U, except in the cases with very cold subsurface water of δT_{50} <-4.0℃. When δT_{50} <-4.0℃, positive SST biases lasted slightly longer, and negative biases were weak (Fig. 11c). This was presumably because the R-MGD analysis requires relatively long time to catch up the dramatic decrease of the actual SST as exemplified in the end of August after the passage of TC Bavi (Fig. 8).

It is likely that three parameters (δT_{50}, V_{max}, and U) are correlated in the western North Pacific. Slow-moving TCs are frequently seen in low-latitude areas where the depth of the OML is much deeper. To avoid the influence of spurious correlation on the magnitude of positive SST bias, we calculated the composite mean of the SST bias for observations during $-150 < d_m < 250$ km and $-0.5 < \Delta t < 3.5$ days (Fig. 12). Fig. 12a clearly shows that the positive bias strongly depends on δT_{50} and V_{max}. The composite mean bias reached as much as +2.23℃ at δT_{50} < -10℃ and V_{max} = 40 m s^{-1}. This indicates that we should be aware of the large SST positive bias in the R-MGD around +2℃, with a width of several hundred kilometers during several days, when a strong TC passes over the region of shallow OML with very cold subsurface water. The positive SST biases tend to be large with slow-moving TCs for a given δT_{50} (Fig. 12b). Therefore, the relatively large SST biases, with fast-moving TCs in Fig. 11g, are merely an artifact due to the fast-moving TCs that tend to appear where δT_{50} is strongly negative. The only exception was the strongly positive bias at U = 21 m s^{-1} and δT_{50} = -6℃. The relevant observations were deployed in 148°E–152°E and

37°N–40°N when TC Sanvu headed north in 2017. It was rare that a TC still had the V_{max} of 65 kt at this latitude, and it caused the large biases.

The multiple linear regression model yields the coefficients as shown below:

$$\text{bias} = -0.1087\delta T_{50} + 0.01402V_{\max} - 0.01398U - 0.2005 \quad (2)$$

This analysis indicates that the positive SST biases highly depend on δT_{50}, while V_{max} and U are also relevant parameters.

For practical applications, it is useful to describe the geographical distribution of SST biases along the TC passage. Fig. 13a shows that the composite mean SST bias for observations during -150 < d_m < 250 km and -0.5 < Δt < 3.5 days generally increases with increasing latitude except the region along Kuroshio current. The composite mean SST bias is approximately +1℃ in the northern part of the East China Sea, Yellow Sea, and Sea of Japan. Positive biases are also notable along the line between 130°E, 24°N, and 156°E, 36°N. This geographical distribution can be basically explained by the climatological features of δT_{50}. The large positive SST biases in the East China Sea, Yellow Sea, and Sea of Japan correspond to the cold subsurface water in these regions where a large SST bias is expected due to a TC easily affecting the SST along its passage. The weak stratification around the Kuroshio and the Kuroshio extension regions can explain the relatively weak positive bias near Okinawan Islands and in the south and east of mainland Japan. In contrast, the composite mean SST bias is relatively small in the south of 20°N.

The composite mean SST bias for observations in -350 < d_m < 350 km and 7.5 < Δt

< 13.5 days is generally negative (figures not shown). Fig. 14. shows the composite mean SST bias for observations during -350 < d_m < 350 km and 7.5 < Δt < 13.5 days, stratified according to the net surface heat fluxes averaged over 5-day prior to the observation. It indicates that the negative SST bias over a wake of the TC passage is more pronounced when the net heat flux from the atmosphere to the ocean is large. It is reasonable because the recovery of SST is rapid in such a case.

5. Bias correction by additional OI

As demonstrated in Sections 3–4, the R-MGD contains TC-related biases lasting for at least two weeks after the TC approach. One potential issue is that short-term fluctuations are mostly removed in the current data processing (Fig. 1, Fig. 8, and Fig. 9). There are potential candidates to consider the short-term fluctuations in the R-MGD analysis using *in-situ* observations, data assimilation, and high-frequency satellite-derived products. As a trial experiment, we conducted a simple additional OI of *in-situ* observations that were obtained within 72 h before the R-MGD analysis time. Since *in-situ* observations are currently used only for adjusting longer than "53-day" scale and large structures of satellite-derived SST estimates, the incorporation of *in-situ* observations within the mentioned 72 h is a potential way to incorporate the short-time-scale fluctuations of the SST fields into R-MGD analysis.

In our additional OI process, the R-MGD was regarded as the first guess field, while the *in-situ* observations within 72 h before the R-MGD analysis time were regarded as the observations. The target region of OI was set to the same as in the previous sections. The basic equation for OI is represented as follows:

$$\mathbf{x}_a = \mathbf{x}_b + \mathbf{B}\mathbf{H}^T \left(\mathbf{H}\mathbf{B}\mathbf{H}^T + \mathbf{R}\right)^{-1} \left(\mathbf{y} - \mathbf{H}\mathbf{x}_b\right) \tag{3}$$

where $\mathbf{x}_a$ is the updated analysis field (hereafter referred to as A-MGD), $\mathbf{x}_b$ is the first guess field representing the R-MGD, $\mathbf{y}$ refers to the *in-situ* observations, $\mathbf{B}$ is the background error covariance matrix, $\mathbf{H}$ is an observation operator, and $\mathbf{R}$ is an observation error covariance matrix. Here, an element of the background error covariance, $\mathbf{B}_{ij}$, is assumed to be a simple function of the distance between two locations as follows:

$$\mathbf{B}_{ij} = \sigma_b^2 \exp\left(-\frac{d_{ij}^2}{2D^2}\right) \tag{4}$$

where ${\sigma_b}^2$ is the magnitude of the background error covariance, d_{ij} is the distance between the two locations, and *D* is the influence radius. $\mathbf{R} = \sigma_o^2 \mathbf{I}$ is the diagonal matrix. Since deviations from the reference values are relatively large in ship-based observations (Xu and Ignatov 2014), we employed the different magnitude of observation errors for ship-based observations alone ($\sigma_{o,\mathrm{ship}}^2$) and for the others ($\sigma_{o,\mathrm{other}}^2$). Note that, from Eqs. (3) and (4), it is obvious that the analysis increment $\mathbf{x}_a - \mathbf{x}_b$ depends on the ratio of σ_o / σ_b, rather than σ_o and σ_b themselves.

For the analysis on day *m*, we first created a single super-observation (sum of the background value and the averaged innovations in a certain size of region and time) by taking an average of misfits between the *in-situ* observations and the R-MGD in a 1° by 1°

bin from 1800 UTC on day *m*-3 to 1800 UTC on day *m*. Here, we considered all best-quality *in-situ* observations regardless of the existence of TCs around the observations. Although we analyzed only one observation for the same platform on one day in Section 4, here we utilized all observations having the "best quality" flag. The current additional OI is computationally inexpensive and only takes a few seconds to create the SST analysis at day *m* with one CPU of AMD EPYC™ 7601.

To reduce the TC-induced biases, we performed a sensitivity test to search for an optimal combination of $\sigma_{o,\mathrm{ship}}/\sigma_b$, $\sigma_{o,\mathrm{other}}/\sigma_b$, and *D* by fitting the analysis value to the independent observations that satisfy -500 < d_m < 500 km and -2 < Δt < 5 days during 2012–2014. For evaluation purpose, observations from 75% of the randomly selected platforms were used for the additional OI. Observations from the remaining platforms were reserved as independent observations, which were not used for the additional OI. Then, we conducted the additional OI for all combinations of $\sigma_{o,\mathrm{ship}}/\sigma_b$, $\sigma_{o,\mathrm{other}}/\sigma_b$, and *D* as shown in Table 1. The smallest root mean square error of the analysis against the independent observations was achieved when $\sigma_{o,\mathrm{ship}}/\sigma_b = 1.6$, $\sigma_{o,\mathrm{other}}/\sigma_b = 1.0$, and *D* = 300 km. Thus, we employ these values to construct A-MGD during 2015–2020.

Fig. 15a shows the analysis increment (A-MGD minus R-MGD) on September 4, 2020, overlapped by dots indicating the SST biases in the R-MGD used for OI, while Fig. 15b–c show the SST fields of the R-MGD and A-MGD on the same day. The analysis increment generally has an opposite sign to the biases in the R-MGD (Fig. 15a), indicating that the additional OI process successfully tried to compensate for the biases. Comparing A-MGD and R-MGD, the SST in A-MGD was found to be lower in the East China Sea, Yellow Sea, Sea of Japan, and around the track of TC Haishen and higher in the South China Sea.

We compared the A-MGD with R-MGD at the location of the coastal moored buoy, as shown in Fig. 8. Although we did not use non-“best quality data” on August 27 in the additional OI process, the rapid SST drop was better reproduced in A-MGD than in R-MGD. In addition, the restoration of the SST in the middle of September was reproduced well in A-MGD. In terms of the power spectrum over five years, A-MGD gained more power in the period <20 days. Its spectrum data was closer to the spectrum of the moored buoys (Fig. 9).

Fig. 16a shows the composite bias of the A-MGD with respect to the *in-situ* observations in a d_m-Δt coordinate, as shown in Fig. 10. The mean bias was substantially reduced over two weeks after the passage of TCs. The maximum positive bias was 0.24℃ and negative bias was -0.17℃, which is much smaller than those in Fig. 10a. The decrease in the bias is also obvious in a TC centered coordinate system (Fig. 16b). Therefore, this approach can diminish the SST biases associated with the TC passage.

As indicated by the reasoning in the present section, the quality of SST analysis can be improved using a simple additional OI easily built upon the existing system with a tiny computational cost. Of course, the current system can be further improved by more appropriate treatment of error covariances, diurnal variation particularly due to clear-sky insolation in a weak wind condition, further quality controls, use of satellite-based short-term fluctuations, and smaller grid spacings. For example, although the influence radius was set at a constant value of 300 km, the dynamic horizontal scale should be adjusted around the coastal region and western boundary currents. The observation error standard deviation σ_o should be dependent on the type of platform and number of observations used for a single super-observation. They are left for future studies. Nevertheless, the current experiment clearly shows that utilizing the *in-situ* observations within 72 hours before the R-MGD analysis time can enhance the representation of the SST field, particularly for short-time scale fluctuations that were mostly removed in the current R-MGD analysis. In addition, we would like to remind that the basic SST structure originally and stability of the system embedded in the R-MGD were not destroyed by this process. This OI merely adds an analysis increment whose scale is determined by the background error covariances and observation density.

6. Weather forecast experiment

6.1 Experimental setting

To quantify the impact of updated SST fields on TC forecasts, we conducted a set of 5-day simulations with R-MGD and A-MGD, using the JMA-NHM (Saito 2012; Saito et al. 2006). The JMA-NHM uses a horizontally explicit and vertically implicit scheme as a dynamical core, with six-category bulk microphysics (Ikawa and Saito 1991), a modified Kain–Fritsch convective scheme (Kain and Fritsch 1990), a clear-sky radiation scheme

(Yabu et al. 2005), and a cloud radiation scheme (Kitagawa 2000). Boundary layer turbulence is determined by the Mellor–Yamada–Nakanishi–Niino level-3 closure model (Nakanishi and Niino 2004). The initial and boundary conditions were given by forecasts of the global spectral model of JMA.

The domain was discretized into 1001 × 1001 grid points centered at 130°E and 30°N. We employed the Lambert conformal projection with grid spacings of 5 km. There were 35 vertical layers, with the model top of 22 km. The time step was 20 s. Our 5-day simulations were conducted once a day when there is a TC at the initial time of 1200UTC from May 2020 to October 2020. We employed R-MGD and A-MGD as the bottom boundary condition, and SSTs were fixed during the run.

We used the methodology by Sakai and Yamaguchi (2005) to track the position of TCs from the 6-hourly outputs, in which the TC's center position was defined as the location of the minimum sea-level pressure (MSLP). Tracking started when a storm was started to be recorded as a TC in the records of RSMC Tokyo best track data. Forecast accuracy was not verified before a storm reaches the threshold of tropical storm status or an extratropical cyclone subjected to transition from the TC. Once the storm experiences the extratropical transition, the tracking was terminated.

6.2 Results

We first investigate the forecasts of TC Maysak and Haishen in 2020, which illustrates the influence of SST biases due to the passage of TCs (Fig. 6). Fig. 17a–b show the TC center positions in the forecasts from August 28 to September 6 with the corresponding RSMC Tokyo best track. Systematic differences in TC tracks were not found in the forecasts with R-MGD and A-MGD. Figs. Fig. 17c–d show the MSLPs for the same cases. In all simulations, TCs were stronger in the forecasts with R-MGD, and the intensity difference became larger with increasing forecast time. The difference of MSLP in the forecasts with R-MGD and A-MGD at the forecast time of 72–96 h was about 5 hPa on average, while the maximum difference was 13 hPa for TC Maysak at the forecast time of 96-h initialized on August 29. The weakly predicted TCs with A-MGD are reasonable because the SST decrease due to the passage of TC Bavi was better reflected in A-MGD and the positive SST biases were reduced at the initial time near the center of predicted TC (Fig. 10). Note that the JMA global-model product was used as our initial condition so that the intense TC cannot be reproduced at the initial time, for example, the forecasts of TC Haishen initialized on September 3. However, the current results show the potential impact of SST product on the TC intensity prediction. To check the versatility of the results, the mean errors were quantified based on the TC forecasts from May 1 to October 31 in 2020. Here, we only verified the cases in which the initial intensity bias did not exceed 25 hPa to remove the extraordinary intensity error around the initial time. Fig. 18 shows that the track forecast skill was not different between forecasts with R-MGD and A-MGD. In contrast, the intensity biases were decreased in the forecasts with A-MGD, contributing to the reduced root mean squared differences in the intensity with respect to the RSMC Tokyo best track (Fig. 18c,d). Although we need further investigations, the current experiments imply the potential benefit for weather forecasts with updated SSTs.

7. Discussion

In Section 5, we demonstrated that the additional OI of the *in-situ* observations reduces the misfit between the in-situ observation and the analyzed SST product. However, the quality of the analysis is not fully guaranteed because the observed SSTs used for the assimilation possibly deviate from true SSTs. To ensure the robustness of the current approach, the observations were separated into two subsets for data assimilation and validation. Namely we conducted an additional experiment in which the OI product by assimilating only ship-based SSTs (referred to as A-MGD-SHIP) and validated against non-ship platforms i.e., drifting buoys, moored buoys, and Argo floats. Fig. 19 shows that the A-MGD-SHIP is better than R-MGD in that the biases were almost halved even against independent observations, although we assign the large observation errors to the ship-based observations. This validation ensures the robustness of the current approach.

8. Concluding remarks

In this study, the potential biases in the near-real-time merged satellite and *in-situ* data global daily Sea surface temperature (SST) of the Japan Meteorological Agency (abbreviated as R-MGD) with respect to *in-situ* observations were quantified along the passage of tropical cyclones (TCs) in the western North Pacific, focusing on the temporal filters used in the R-MGD analysis. The case study and composite analysis exhibited that positive biases occurred when the SST dropped rapidly in a few days after the passage of TCs, while negative biases typically occurred when the SST was restoring one week after the passage. During August–September 2020, the biases reached more than +2℃. It is explained by the availability of the data as the near-real-time product and the exceedingly gentle temporal changes in the R-MGD system, which filters out short-time-scale fluctuations that occurred during the “less than 27-day” period. The positive SST bias is largely associated with the cold subsurface water and intense TCs, and thus, the positive biases are notable in the East China Sea, Yellow Sea, Sea of Japan, and in the southeast of Japan and Ryukyu Islands except around the Kuroshio and the Kuroshio extension regions. In fact, storm-induced SST biases in the composite analysis might be underestimated because some actual observations were classified into non-“best quality” categories due to the rapid changes. This issue is discussed in Supplement 3.

It is encouraging that the OI of the *in-situ* observations obtained within 72 h prior to the R-MGD analysis time can alleviate these biases because this process can add more information on short-term fluctuations. Because our additional OI system is very simple, it strongly suggests that the consideration of short-term fluctuations is indispensable to diminish the SST biases. Although the proposed approach is computationally cheap and can be easily implemented upon the existing system, we do not insist that this approach is the best for improving the quality of SST analysis. An alternative approach is to assign more weights to short-term scale features from satellites or to use a sophisticated oceanic data assimilation technique such as four-dimensional variational data assimilation system that employs the ocean model dynamics to constrain the SST field where the observations are not available. Furthermore, we can assign the previous SST analysis as a first guess and digest the satellite and *in-situ* observations within a few days through the optimal interpolation as in Operational Sea Surface Temperature and Sea Ice Analysis (OSTIA), which suffer much less TC-induced SST biases (Supplement 2). In May 2021, the JMA publicized a future plan to incorporate short-term-fluctuations in the global SST analysis by replacing MGDSST with the global HIMSST (https://www.jma.go.jp/jma/kishou/shingikai/kondankai/suuchi_model_kondankai/part5/part5-shiryo1.pdf). Although the SST biases in HIMSST are slightly smaller than in R-MGD (Supplement 4), a careful comparison of various approaches in terms of the benefits and risks is preferrable toward the further improvements.

The SST biases in R-MGD after the passage of TCs may not be favorable in weather and ocean forecasts because the biases bring about persistent errors in the JMA systems. To quantify the contribution of the updated SST on weather forecasts, we conducted a 51 5-day forecasts with R-MGD and A-MGD. The updated SST generally yields the better TC intensity forecasts. However, the evaluation for predicting high-impact weather events seems to require more samples, which will be a future topic. Also, further improvements may come from the data assimilation system inheriting the updated weather fields as the first guess in the next cycle and the lateral boundary condition out of the improved global model forecasts.

We have not evaluated the forecast skills of heavy rainfall events with a high-resolution model. It is another future topic that should be investigated in the near future. For example, heavy rainfall events in Japan are very sensitive to the SST in the East China Sea or Sea of Japan (Iizuka and Nakamura 2019; Manda et al. 2014; Moteki and Manda 2013) as well as the TC forecasts (Emanuel 1986; Ito and Ichikawa 2021; Nayak and Takemi 2019). The Northern-Kyushu heavy rainfall event in 2017, Western-Japan heavy rainfall event in 2018, and TC Haishen in 2020 occurred just after the passage of TCs Nanmadol (in 2017), Prapiroon (in 2018), and Bavi and Maysak (in 2020) in the East China Sea and Sea of Japan, respectively. The prediction skill of such events could be enhanced if the high-quality SST analyses were used. As such, the bias of near-real-time SST should be resolved not only for daily forecasts but also for disaster prevention and mitigation.

Although we have mainly focused on the TC-related SST biases of R-MGD in the western North Pacific, the biases in the other basins and products are described in the Supplements. Supplement 1 shows that D-MGD contains negative (positive) biases at the analysis time before (after) the closest approach of a TC as expected in Fig. 2c-d. Supplement 2 shows the global analysis of TC-related SST biases in R-MGD and OSTIA. It shows the biases of R-MGD were found in all basins, while the biases are much smaller in OSTIA. Supplement 3 discusses the possible underestimation of SST biases in this work airing from the inappropriate QCs of the *in-situ* dataset. When the TC-induced SST decrease is very rapid, the *in-situ* SST observations can be regarded as suspicious presumably due to the large deviation from the background SST. Thus, the biases with respect to the true SST might be larger than those in the main text. In Supplement 4, the monthly mean SST errors in A-MGD are smaller than in R-MGD even with the observations outside of TCs. Supplement 5 shows that the time lag between the SST analysis time and the initial time of JMA global model forecasts can increase SST biases in the forecast system. In turn, the frequent update of SST can slightly decrease the SST biases. Supplement 6 describes the TC-related SST biases in HIMSST. The biases of HIMSST are slightly smaller compared to those of R-MGD. The assimilation of *in-situ* observations recorded within 72 h through additional optimal interpolation further decrease these biases. These Supplements are useful for a practical application and further developments.

Supplement

Supplement 1 shows the SST biases in D-MGD. Supplement 2 shows the global analysis of TC-related SST biases in R-MGD and OSTIA. Supplement 3 analyzes the SST biases including the low-quality dataset. Supplement 4 describes the SST errors including the observations outside of TCs. Supplement 5 shows the dependence of SST biases on the reference time. Supplement 6 describes the TC-related SST biases in HIMSST.

Acknowledgments

We thank Dr. Naoki Hirose, Dr. Masahiro Sawada, Dr. Soichiro Hirano, Dr. Udai Shimada, Dr. Yosuke Fujii, Dr. Takahiro Toyoda, Dr. Kei Sakamoto, Ms. Mieko Seki, and the JMA Office of Marine Prediction for valuable information and comments. This work was supported by the University of the Ryukyus Research Project Promotion Grant (Strategic Research Grant 18SP01302) and MEXT KAKENHI (Grant JP18H01283). SSTs at the KEO buoy were provided by the OCS Project Office of NOAA/PMEL. AMSR2 data used in this paper was supplied by the GHRSST Server, Japan Aerospace Exploration Agency. This work is done for the author’s research purposes and should not be regarded as official JMA views.

List of Tables

List of Figures

and (d-f) R-MGD during (a,d) August 19-21, (b,e) September 3-5, and (c,f) September 13-15. Thick solid and thin broken lines represent TC tracks.

Fig. 8. Comparison of SST in the KMA moored buoy (black), R-MGD (red), A-MGD (blue; explained in Section 5), and OSTIA (orange). Gray closed circles and crosses respectively represent 6-hourly SST in the moored buoy with a flag of “best-quality” and non-“best-quality,” while the black line indicates a daily-mean value. The climatological SST on the day of the year is shown in a purple dotted line. Green closed circles represent the standard GCOM-W1/AMSR2 SST product based on the microwave satellites at the closest location. Three upside-down triangles represent the time of the closest approach of TCs Bavi, Maysak, and Haishen.

Fig. 9. The power spectrum of SST anomalies (with respect to the climatology) from July 2015 through June 2020: Buoy (black), R-MGD (red), A-MGD (blue; see Section 5), and AMSR2 (green) at (a) Marado and (b) KEO. The power spectrum is shown for the buoy location in Buoy, and the nearest grid point in R-MGD, A-MGD, and AMSR2. Light thin lines indicate the original power spectrum, while the thick dense lines indicate the power spectrum smoothed over neighboring 21 frequencies.

Fig. 10. Composite bias of R-MGD with respect to in-situ observations in (a) d_m-Δt coordinate and (b) TC-centered coordinate. The statistically significant bias with 95 % confidence level is shown by broken contours.

Fig. 11. Same as Fig. 10a but classified according to (a)–(c) δT_{50} (deviation of ocean temperature at 50-m depth, with respect to the ocean temperature at 1 m), (d)–(f) V_{max}, and (g)–(i) TC translation speed. Note that the color bar is different from that used in Fig. 10a.

Fig. 12. Composite mean SST biases obtained during -150 < d_{m} < 250 km and -0.5 < Δt < 3.5 days, with a combination of two parameters among δT_{50}, TC translation speed, and V_{max}. A white blank indicates that the number of available *in-situ* observations is less than 10. Note that the leftmost bins in (a) and (b) correspond to $\delta T_{50} < -9$℃.

Fig. 13. Composite mean SST biases for -0.5 < Δt < 3.5 days and -150 < d_{m} < 250 km. White blank indicates that the number of available *in-situ* observations is less than 10 at each grid point.

Fig. 14. Composite mean SST biases obtained during -350 < dm < 350 km and 7.5 < Δt < 13.5 days, stratified according to the net surface heat flux averaged over 5 days prior to the observation. Positive net surface heat flux corresponds to the transport of energy from the atmosphere to the ocean.

Fig. 15. (a) Analysis increment of SSTs in A-MGD with respect to R-MGD overlapped by dots indicating SST biases used for additional OI process. SSTs in (b) R-MGD and (c) A-MGD. Black lines indicate the TC tracks.

Fig. 16. Same as Fig. 10 but for A-MGD.

Fig. 17. RSMC Tokyo best track data (black dots) overlaid by the daily forecasts with R-MGD (red) and A-MGD (blue). (a)(b) track and (c)(d) MSLP (in hPa) for TC Maysak and Haishen.

Fig. 18. (a) Number of validated cases for TC forecasts. (b) Mean track forecast error (in km). (c) Mean bias in the minimum sea level pressure forecasts (in hPa). (d) root mean squared difference of the minimum sea level pressure forecasts (in hPa).

Fig. 19. SST bias in (a) R-MGD and (b) A-MGD-SHIP as Fig. 10a validated against in-situ observations except ship-based SST.

Table 1. Parameter values tested for finding the optimal combination in the additional OI.

parameter	values
$\sigma_{o,\mathrm{ship}}/\sigma_b$	0.4, 0.6, 0.8, 1.0, 1.2, 1.4, 1.6, 1.8
$\sigma_{o,\mathrm{other}}/\sigma_b$	0.4, 0.6, 0.8, 1.0, 1.2, 1.4, 1.6, 1.8
D	100 km, 200 km, 300 km, 400 km, 500 km

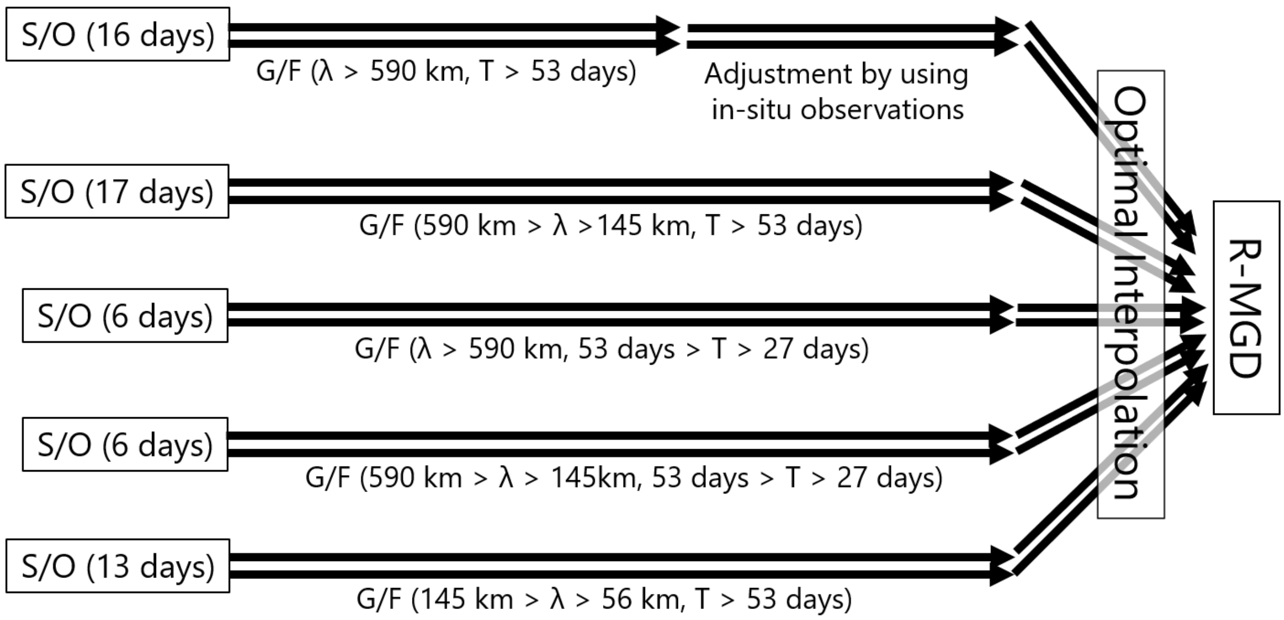

Fig. 1. Procedure used to produce R-MGD carried out by the Japan Meteorological Agency; as of December 11, 2020). S/O represents quality-controlled and preprocessed satellite observations; G/F represents Gaussian filtering. Precise definition of filtering scales is given in Section 1.

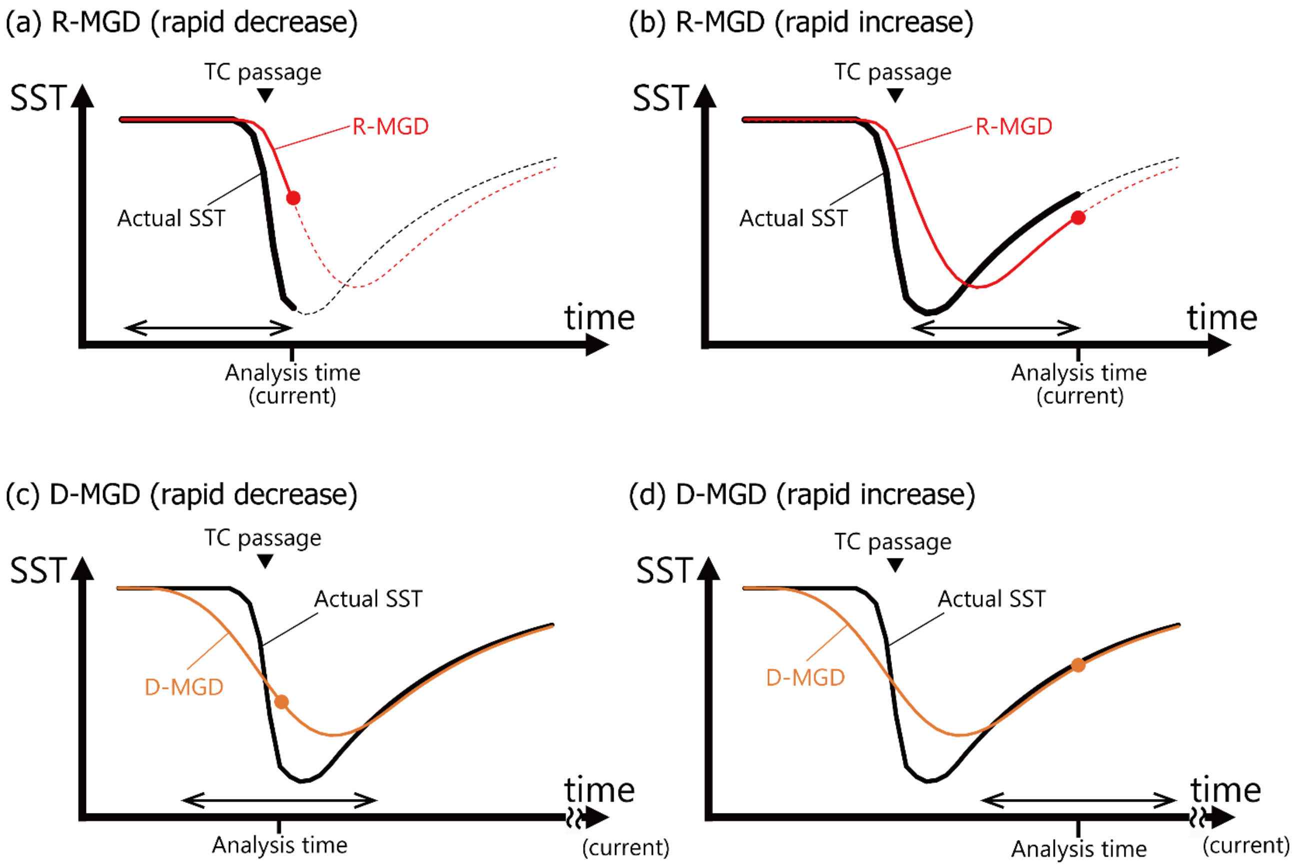

Fig. 2. Schematic illustration of the expected SST biases in R-MGD and D-MGD for hypothetical SST change associated with the passage of a TC. Black solid lines indicate the raw SSTs known at the time of the analysis, while red and orange solid lines indicate the R-MGD and D-MGD. Broken lines indicate the future SSTs that are not available at the time of the analysis. The two-sided arrows indicate the period of a raw SST used for constructing the analysis products (R-MGD or D-MGD). Closed circles indicate the SST analysis determined by the raw SSTs. It is assumed that the SST recovers to the original SST in a long run.

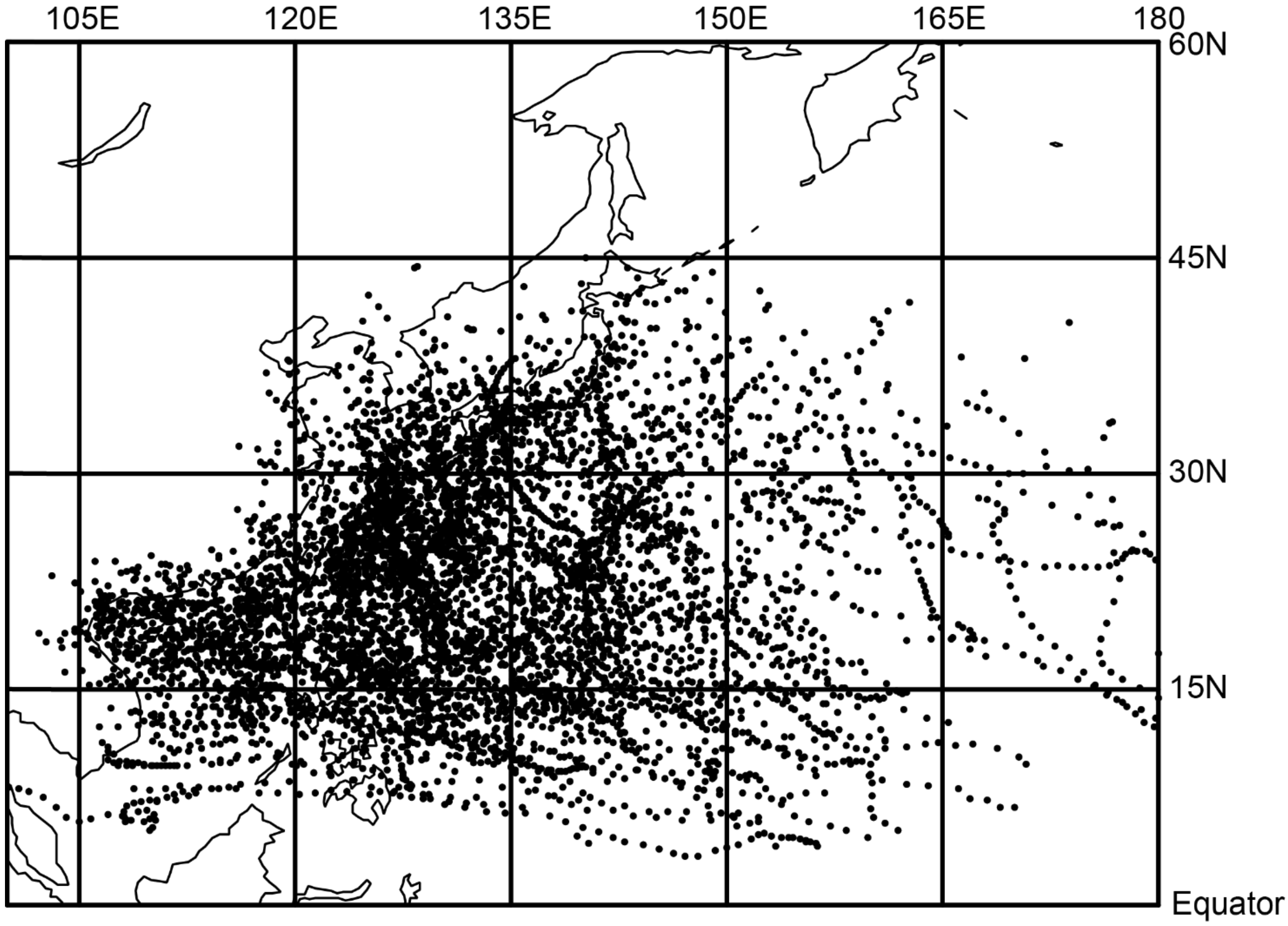

Fig. 3. The 6-hourly center positions in the RSMC Tokyo best track used for the composite analysis.

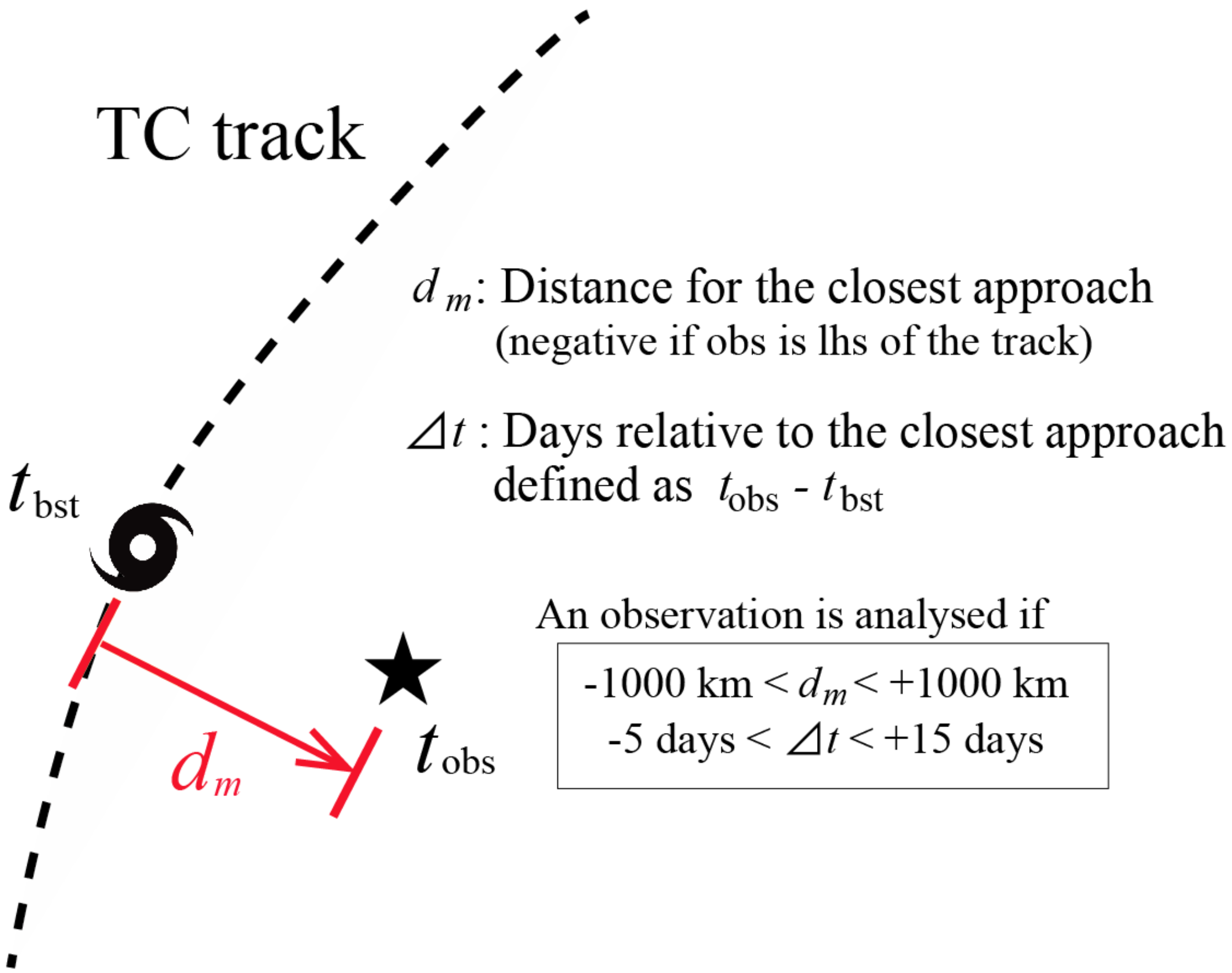

Fig. 4. Schematic illustration of definition of d_m and Δt; t_{obs} is the observed time, t_{bst} is the time of the closest approach of a TC recorded in the RSMC Tokyo best track.

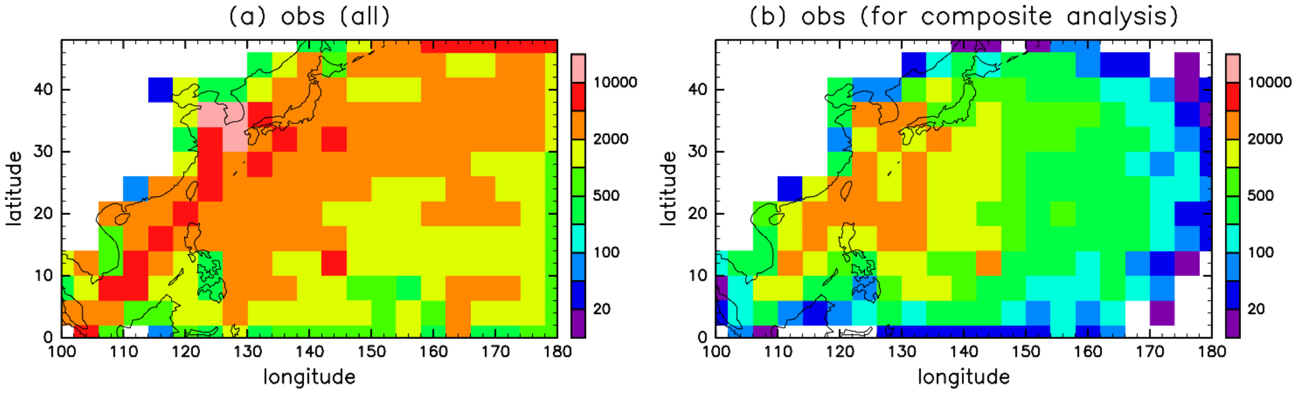

Fig. 5. (a) The number of observations, sampling only one data point from the same platform on one day. (b) Same as (a) but those used for the composite analysis, satisfying -5 < Δt < +15 days and -1000 < d_m < 1000 km.

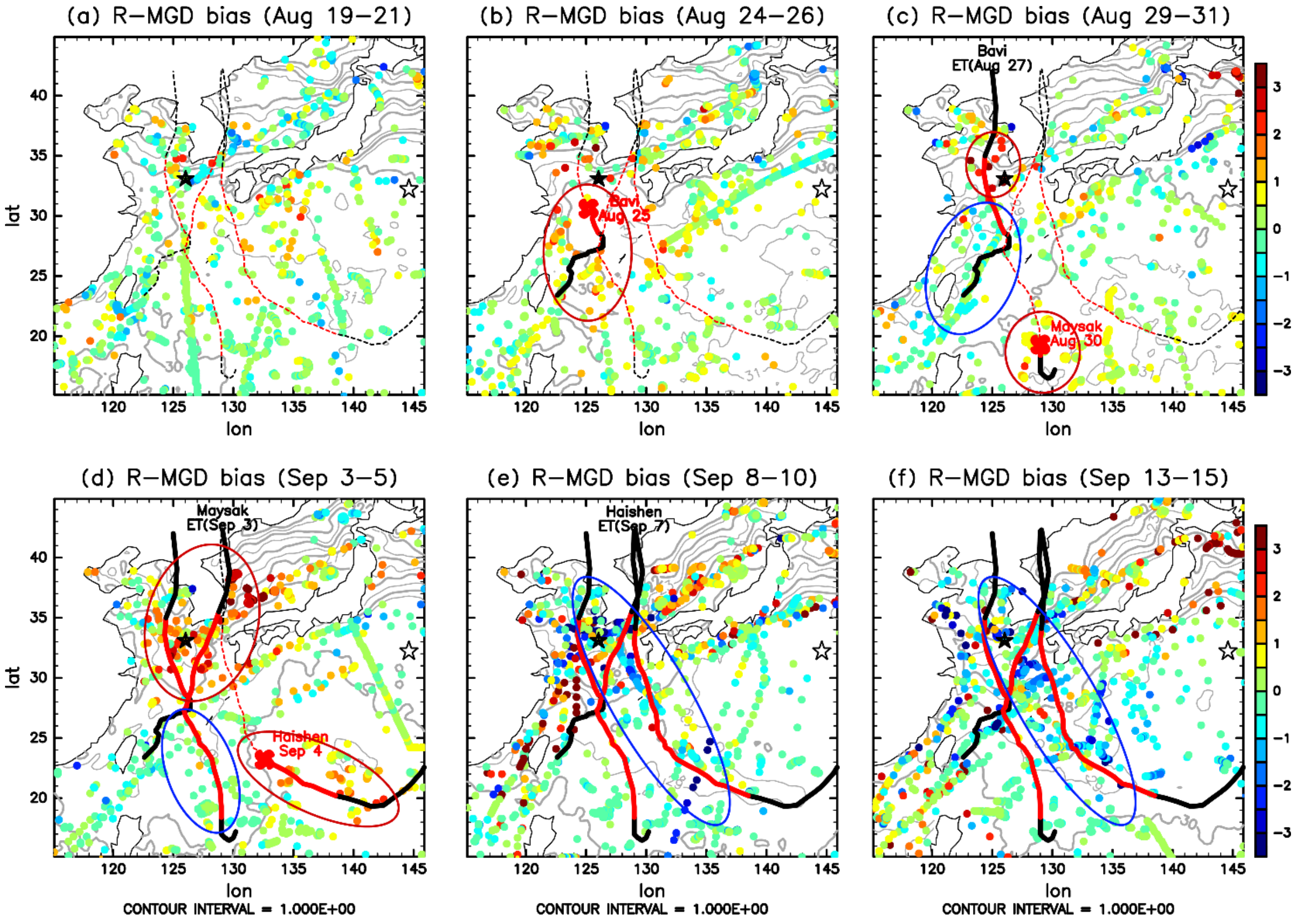

Fig. 6. Bias in R-MGD with respect to *in-situ* observations (colored dots). Each plot uses *in-situ* observations in 3 days: (a) August 19–21, (b) August 24–26, (c) August 29–31, (d) September 3–5, (e) September 8–10, and (f) September 13–15. Thick solid and think broken lines represent TC tracks, and a part of lines in red indicates the period when V_{max} was 75 kt or more. The best track data is not considered before a TC reaches the threshold of tropical storm status or an extratropical cyclone subjected to transition from the TC. Dates of extratropical transition are indicated by ET. Major positive (negative) biases along the passage of TCs are indicated by red (blue) ellipses. Gray contours indicate R-MGD. The contour interval is 1℃. A closed asterisk indicates the location of the KMA moored buoy (ID 22107), while an open asterisk indicates the location of the KEO buoy. Note that if available, more than one data are plotted from the same platform in one day.

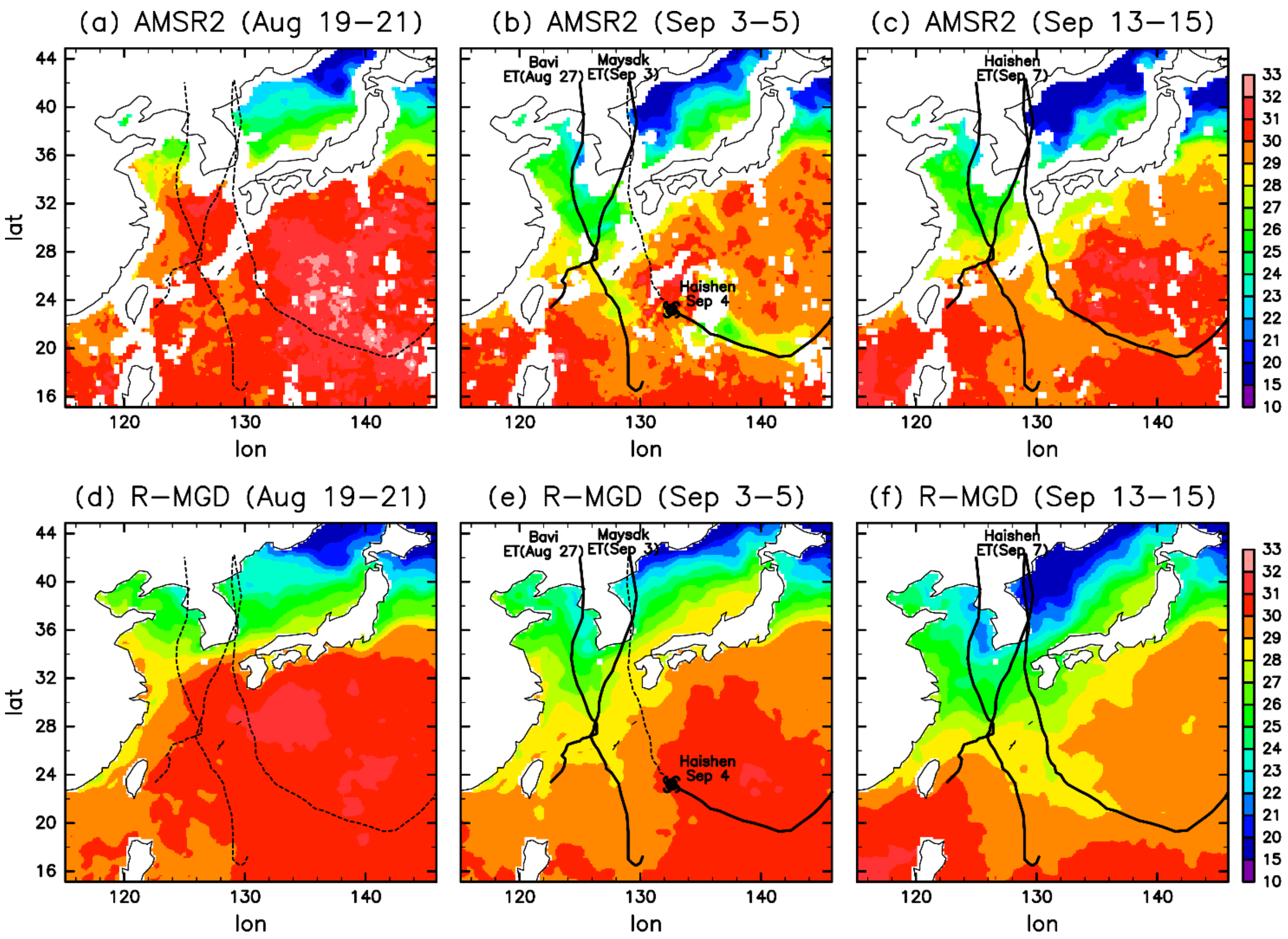

Fig. 7. Three-day mean of (a-c) Microwave satellite-based SST from GCOM-W1/AMSR2 and (d-f) R-MGD during (a,d) August 19-21, (b,e) September 3-5, and (c,f) September 13-15. Thick solid and thin broken lines represent TC tracks.

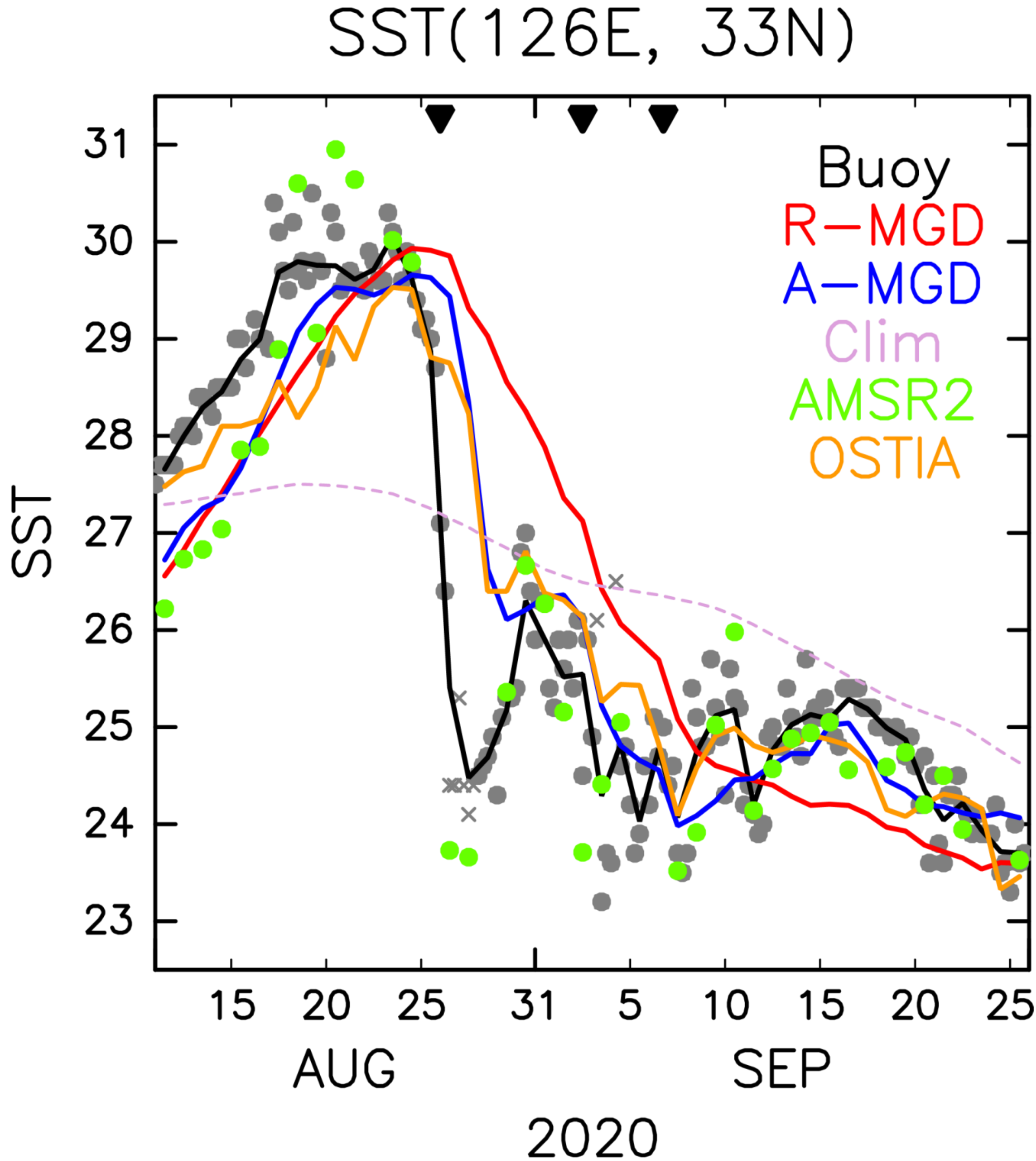

Fig. 8. Comparison of SST in the KMA moored buoy (black), R-MGD (red), A-MGD (blue; explained in Section 5), and OSTIA (orange). Gray closed circles and crosses respectively represent 6-hourly SST in the moored buoy with a flag of "best-quality" and non-"best-quality," while the black line indicates a daily-mean value. The climatological SST on the day of the year is shown in a purple dotted line. Green closed circles represent the standard GCOM-W1/AMSR2 SST product based on the microwave satellites at the closest location. Three upside-down triangles represent the time of the closest approach of TCs Bavi, Maysak, and Haishen.

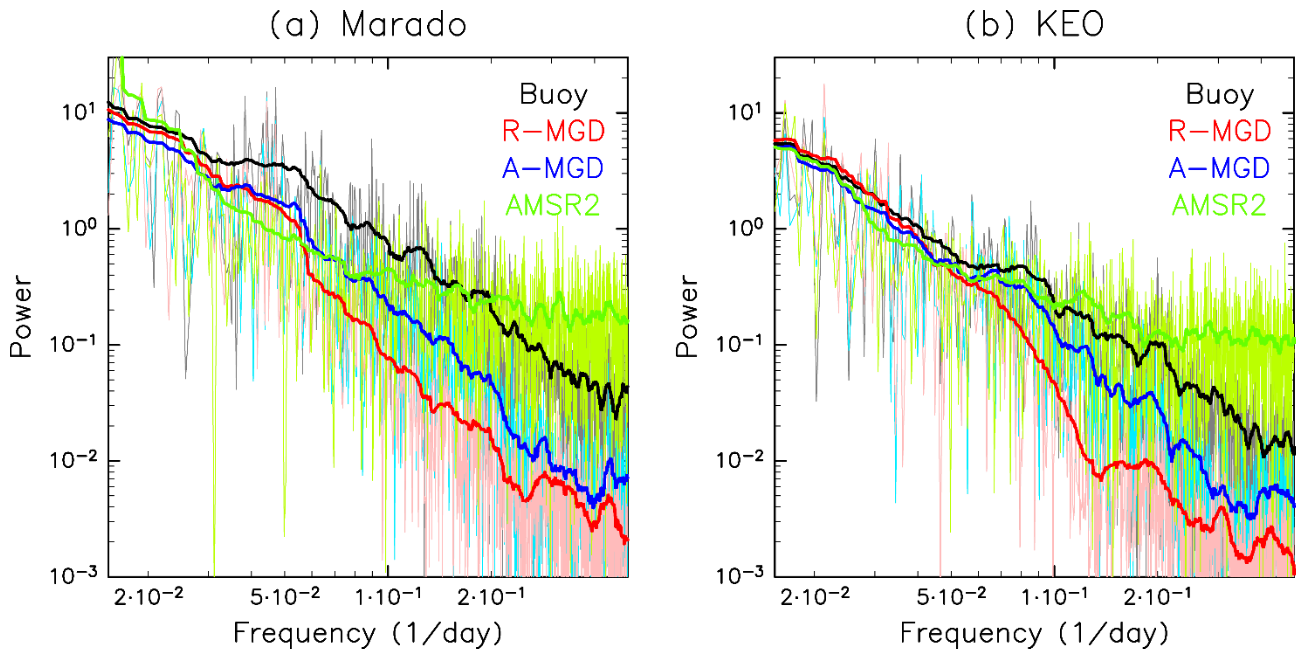

Fig. 9. The power spectrum of SST anomalies (with respect to the climatology) from July 2015 through June 2020: Buoy (black), R-MGD (red), A-MGD (blue; see Section 5), and AMSR2 (green) at (a) Marado and (b) KEO. The power spectrum is shown for the buoy location in Buoy, and the nearest grid point in R-MGD, A-MGD, and AMSR2. Light thin lines indicate the original power spectrum, while the thick dense lines indicate the power spectrum smoothed over neighboring 21 frequencies.

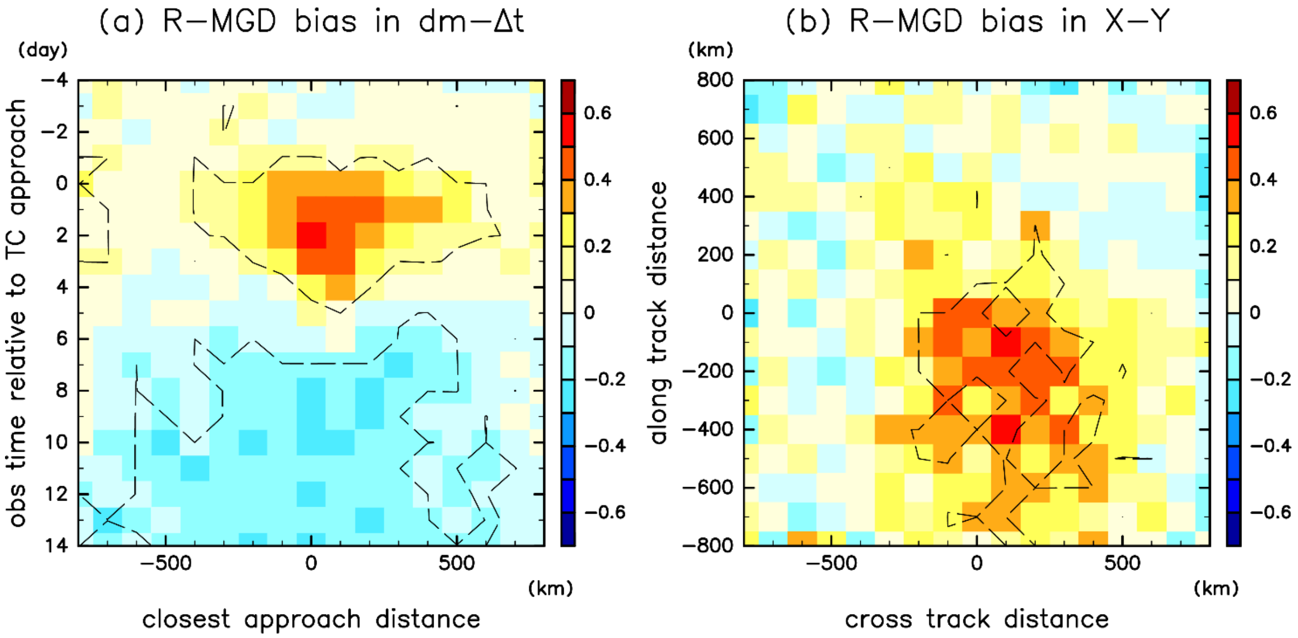

Fig. 10. Composite bias of R-MGD with respect to in-situ observations in (a) d_m-Δt coordinate and (b) TC-centered coordinate. The statistically significant bias with 95 % confidence level is shown by broken contours.

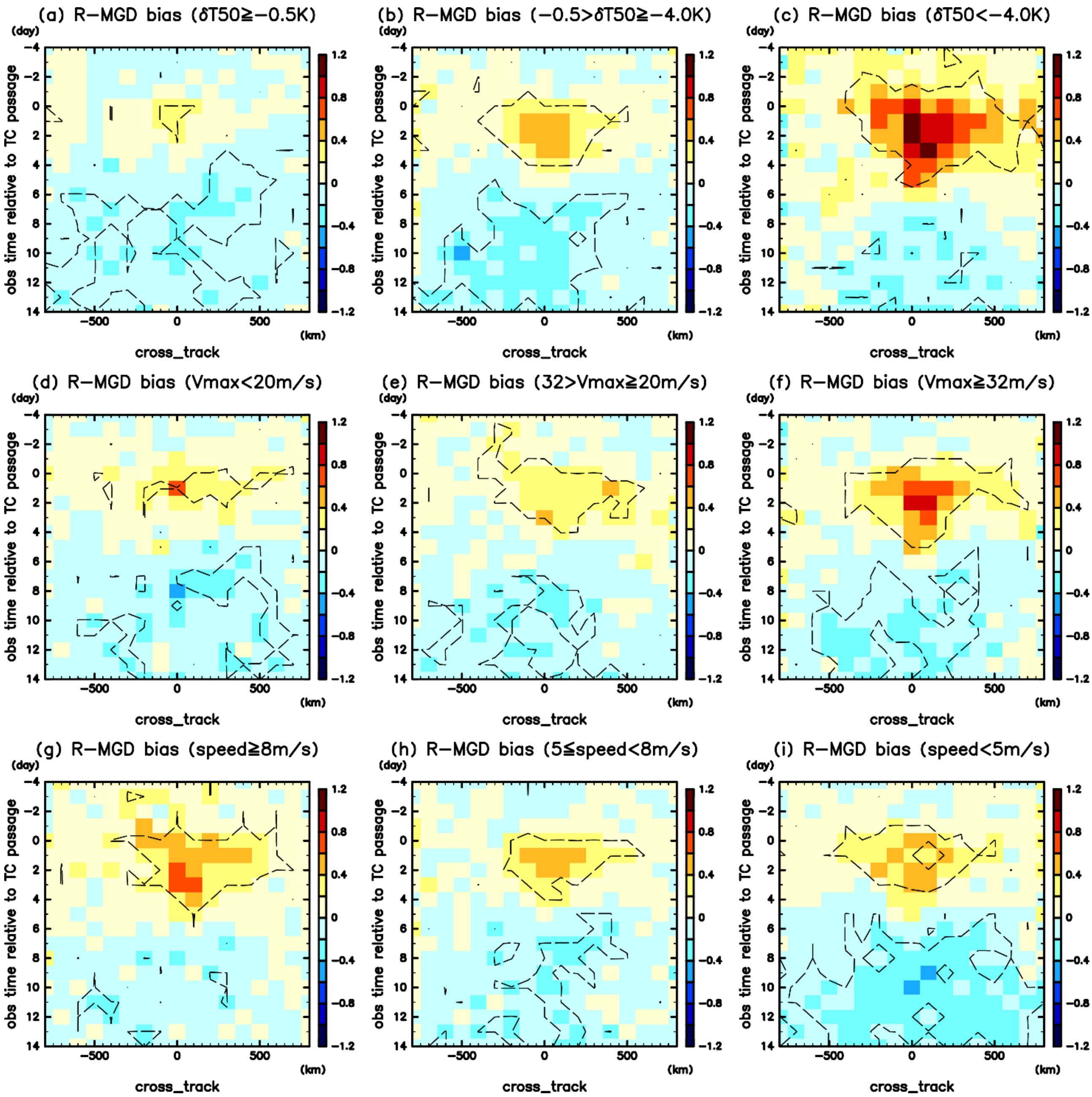

Fig. 11. Same as Fig. 10a but classified according to (a)–(c) δT_{50} (deviation of ocean temperature at 50-m depth, with respect to the ocean temperature at 1 m), (d)–(f) V_{max}, and (g)–(i) TC translation speed. Note that the color bar is different from that used in Fig. 10a.

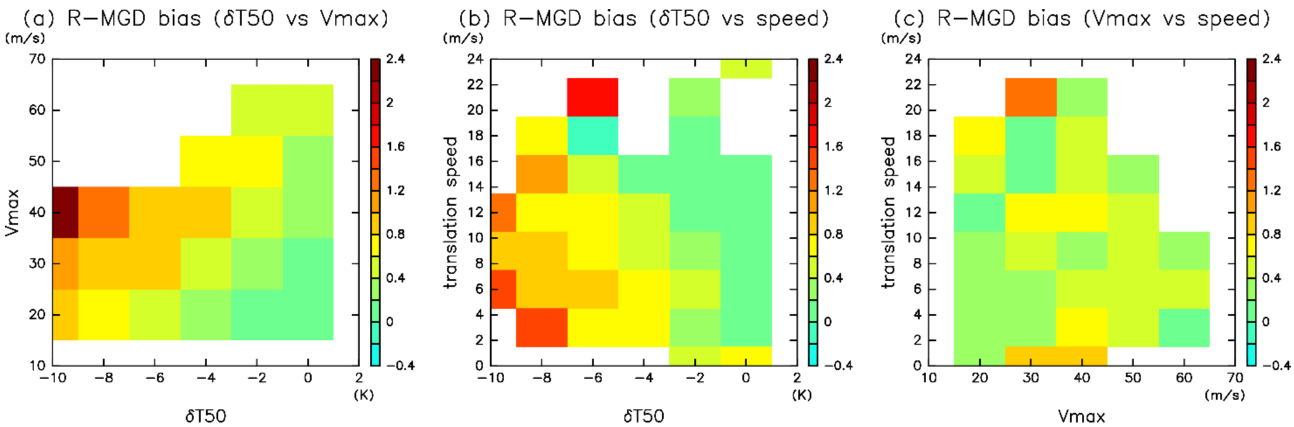

Fig. 12. Composite mean SST biases obtained during -150 < d_m < 250 km and -0.5 < Δt < 3.5 days, with a combination of two parameters among δT_{50}, TC translation speed, and V_{max}. A white blank indicates that the number of available *in-situ* observations is less than 10. Note that the leftmost bins in (a) and (b) correspond to δT_{50} < -9℃.

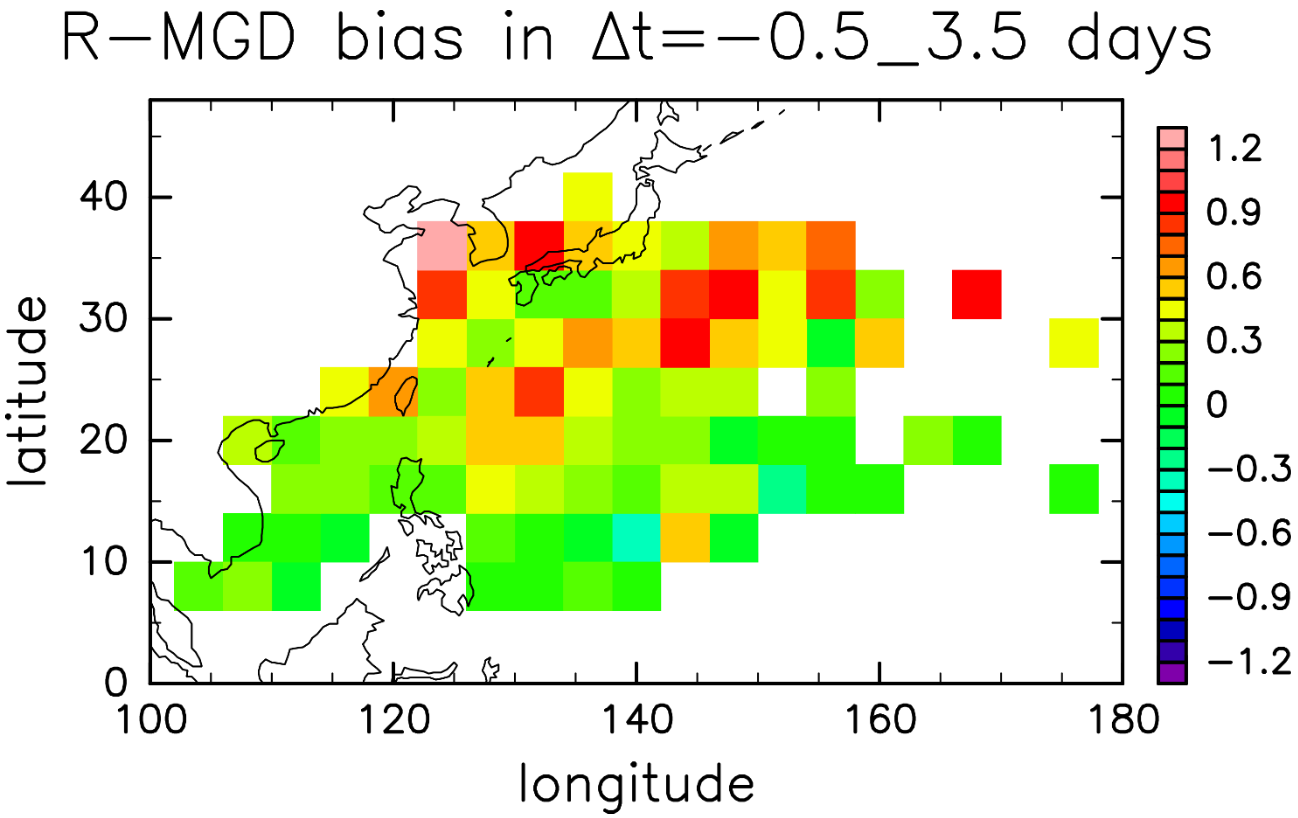

Fig. 13. Composite mean SST biases for -0.5 < Δt < 3.5 days and -150 < d_m < 250 km. White blank indicates that the number of available *in-situ* observations is less than 10 at each grid point.

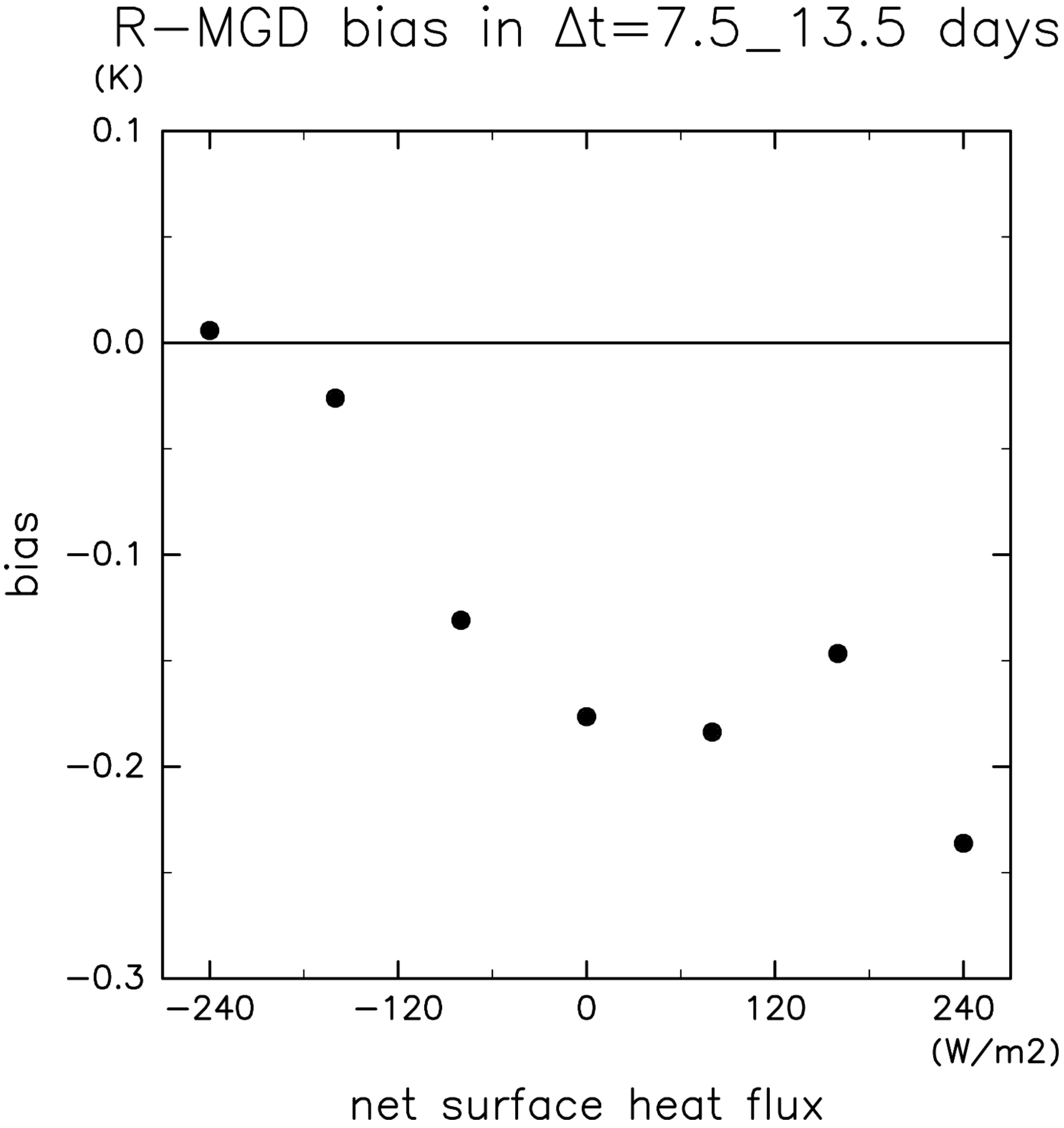

Fig. 14. Composite mean SST biases obtained during -350 < dm < 350 km and 7.5 < Δt < 13.5 days, stratified according to the net surface heat flux averaged over 5 days prior to the observation. Positive net surface heat flux corresponds to the transport of energy from the atmosphere to the ocean.

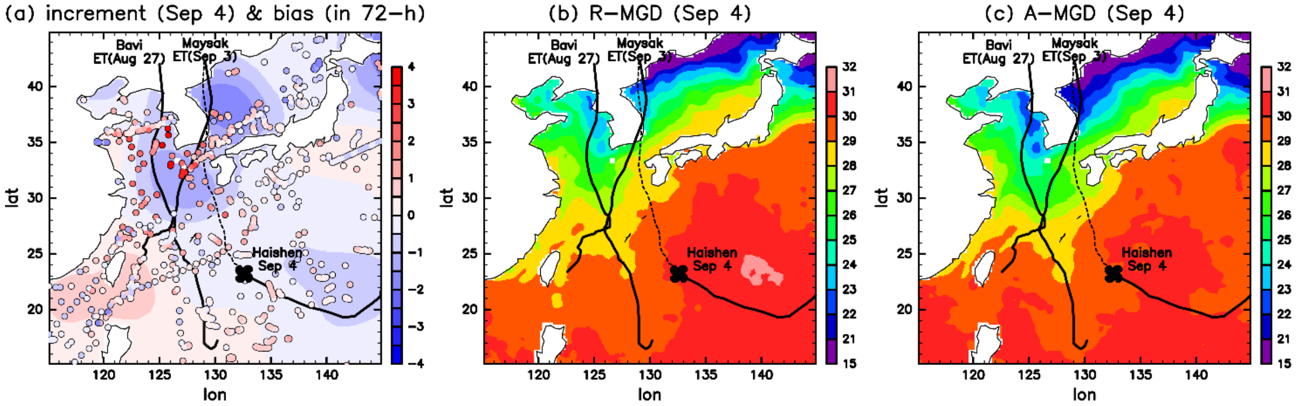

Fig. 15. (a) Analysis increment of SSTs in A-MGD with respect to R-MGD overlapped by dots indicating SST biases used for additional OI process. SSTs in (b) R-MGD and (c) A-MGD. Black lines indicate the TC tracks.

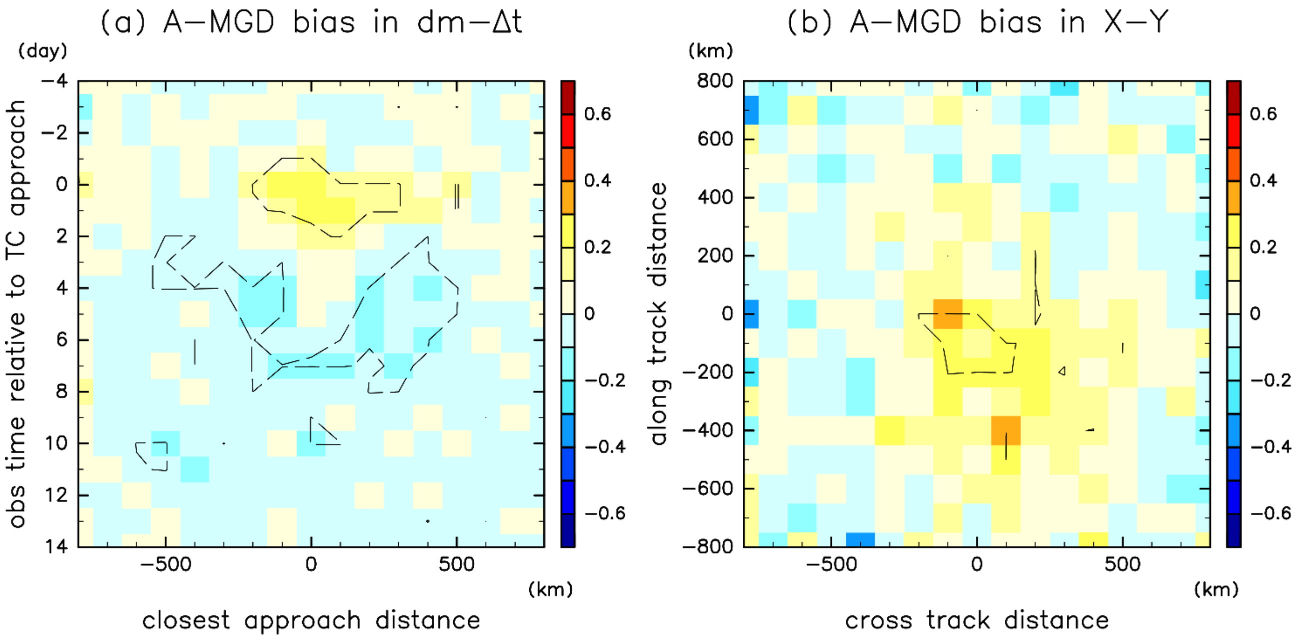

Fig. 16. Same as Fig. 10 but for A-MGD.

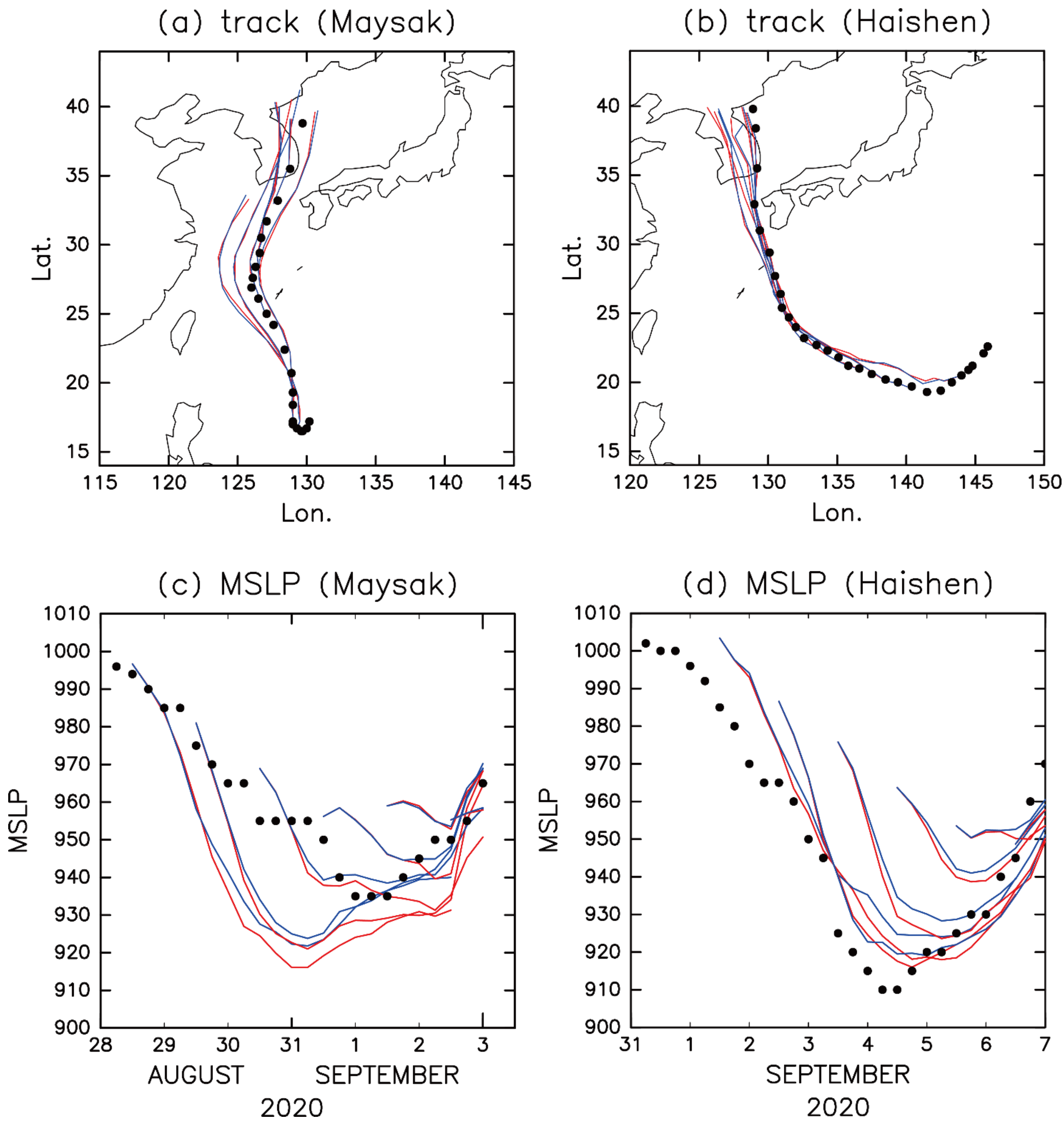

Fig. 17. RSMC Tokyo best track data (black dots) overlaid by the daily forecasts with R-MGD (red) and A-MGD (blue). (a)(b) track and (c)(d) MSLP (in hPa) for TC Maysak and Haishen.

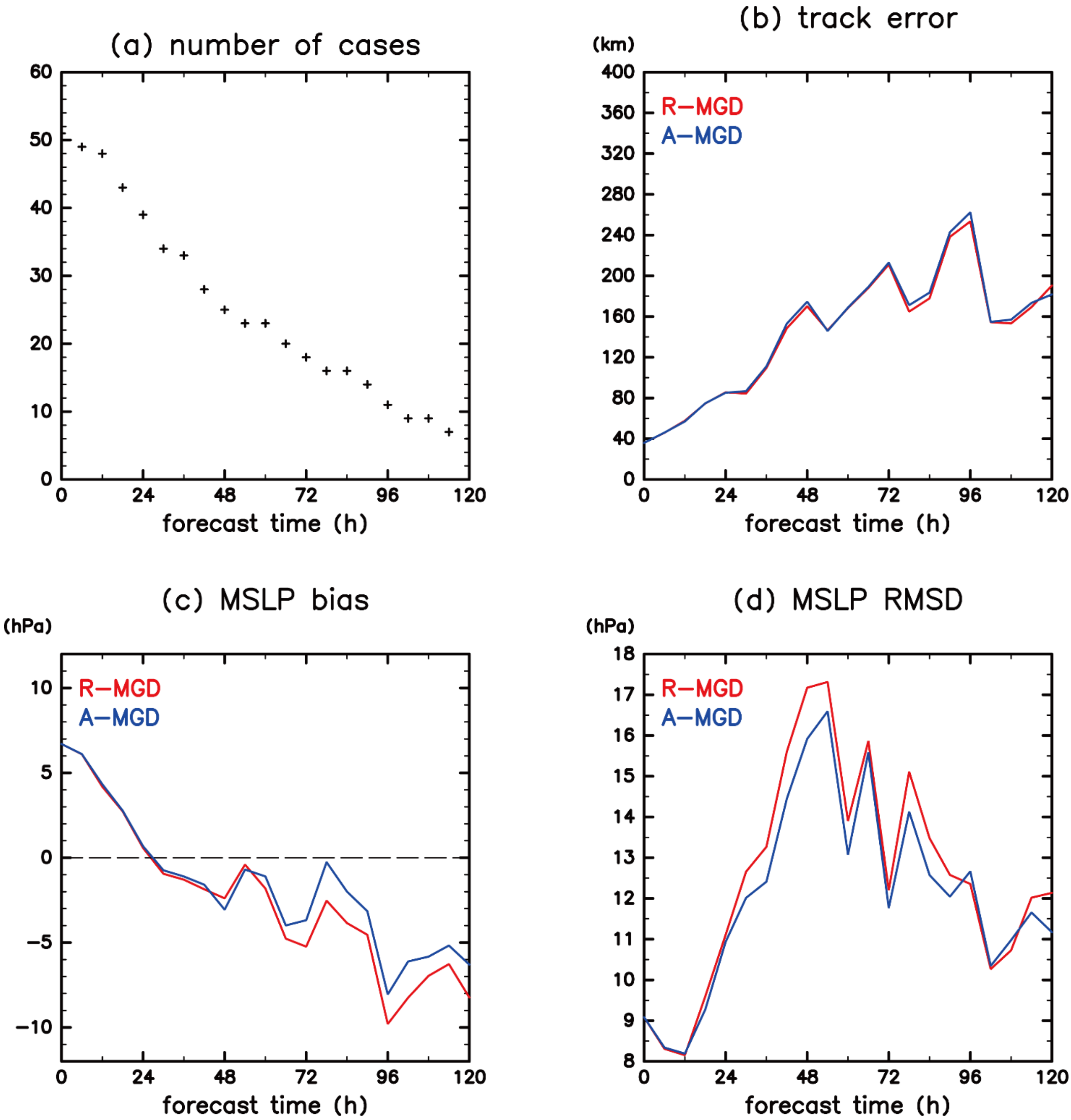

Fig. 18. (a) Number of validated cases for TC forecasts. (b) Mean track forecast error (in km). (c) Mean bias in the minimum sea level pressure forecasts (in hPa). (d) root mean squared difference of the minimum sea level pressure forecasts (in hPa).

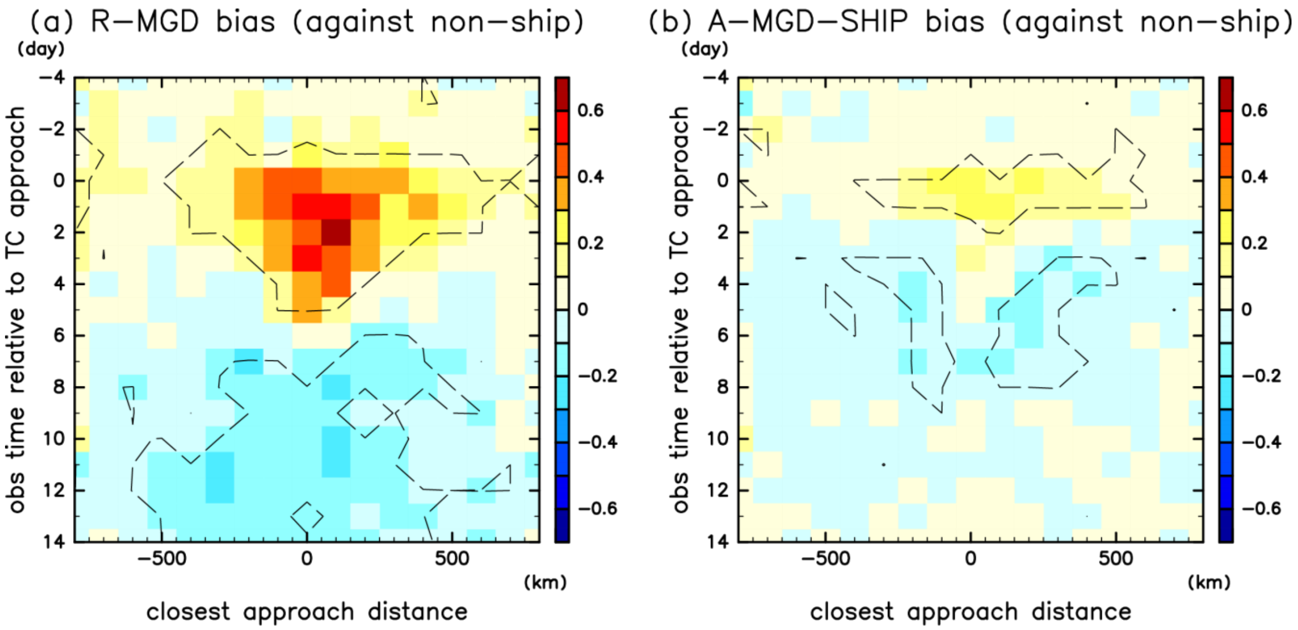

Fig. 19. SST bias in (a) R-MGD and (b) A-MGD-SHIP as Fig. 10a validated against *in-situ* observations except ship-based SST.

References

Dare, R. A., and J. L. McBride, 2011: Sea surface temperature response to tropical cyclones. *Mon. Wea. Rev.*, **139,** 3798-3808.

Donlon, C. J., M. Martin, J. Stark, J. Roberts-Jones, E. Fiedler, and W. Wimmer, 2012: The operational sea surface temperature and sea ice analysis (OSTIA) system. *Remote Sensing of Environment*, **116,** 140-158.

Emanuel, K. A., 1986: An air-sea interaction theory for tropical cyclones. Part I: Steady-state maintenance. *J. Atmos. Sci.*, **43,** 585-605.

Hirose, N., and Coauthors, 2019: Development of a new operational system for monitoring and forecasting coastal and open-ocean states around Japan. *Ocean Dynamics*, **69,** 1333-1357.

Huang, B., W. Wang, C. Liu, V. Banzon, H.-M. Zhang, and J. Lawrimore, 2015: Bias adjustment of AVHRR SST and its impacts on two SST analyses. *Journal of Atmospheric and Oceanic Technology*, **32,** 372-387.

Iizuka, S., and H. Nakamura, 2019: Sensitivity of midlatitude heavy precipitation to SST: A case study in the Sea of Japan area on 9 August 2013. *J. Geophys. Res. Atmos.*, **124,** 4365-4381.

Ikawa, M., and K. Saito, 1991: Description of a nonhydrostatic model developed at the Forecast Research Department of the MRI. *Technical Reports***,** 238 pp.

Ishii, M., A. Shouji, S. Sugimoto, and T. Matsumoto, 2005: Objective analyses of sea-surface temperature and marine meteorological variables for the 20th century using ICOADS and the Kobe collection. *International Journal of Climatology: A Journal of the Royal Meteorological Society*, **25,** 865-879.

Ito, K., and H. Ichikawa, 2021: Warm ocean accelerating tropical cyclone Hagibis (2019) through interaction with a mid-latitude westerly jet. *SOLA***,** 17A-001.

Ito, K., T. Kuroda, K. Saito, and A. Wada, 2015: Forecasting a large number of tropical cyclone intensities around Japan using a high-resolution atmosphere-ocean coupled model. *Wea. Fore.*, **30,** 793-808.

Jeong, Y. Y., I.-J. Moon, and S.-H. Kim, 2013: A study on upper ocean response to typhoon Ewiniar (0603) and its impact. *Atmosphere*, **23,** 205-220.

JMA, cited 2021: Climate change monitoring report 2016. [Available online at https://www.jma.go.jp/jma/en/NMHS/ccmr/ccmr2016_high.pdf.]

——, cited 2021: Outline of the operational numerical weather prediction at the Japan Meteorological Agency (March 2019). [Available online at http://www.jma.go.jp/jma/jma-eng/jma-center/nwp/outline2019-nwp/index.htm.]

——, 2021: *Annual Report of Numerical Prediction Development Center 2020.* JMA Numerical Prediction Development Center, 158 pp.

Kain, J. S., and J. M. Fritsch, 1990: A one-dimensional entraining/detraining plume model and its application in convective parameterization. *J. Atmos. Sci.*, **47,** 2784-2802.

Kanada, S., H. Aiki, K. Tsuboki, and I. Takayabu, 2021: Future Changes of a Slow-moving Intense Typhoon with Global Warming: A Case Study using a regional 1-km-mesh atmosphere–ocean coupled model. *SOLA***,** 17A-003.

Kent, E. C., P. K. Taylor, B. S. Truscott, and J. S. Hopkins, 1993: The accuracy of Voluntary Observing Ships' meteorological observations-Results of the VSOP-NA. *Journal of Atmospheric and Oceanic Technology*, **10,** 591-608.

Kitagawa, H., 2000: Radiation processes. *Separate volume of annual report of JMA-NPD*, **46,** 16-31.

Kobayashi, S., and Coauthors, 2015: The JRA-55 reanalysis: General specifications and basic characteristics. *Journal of the Meteorological Society of Japan. Ser. II*, **93,** 5-48.

Kurihara, Y., T. Sakurai, and T. Kuragano, 2006: Global daily sea surface temperature analysis using data from satellite microwave radiometer, satellite infrared radiometer and in-situ observations (in Japanese). *Weather service bulletin (sokko-jiho)*, **73,** S1-18.

Kusunoki, S., and R. Mizuta, 2008: Future changes in the Baiu rain band projected by a 20-km mesh global atmospheric model: Sea surface temperature dependence. *SOLA*, **4,** 85-88.

Lin, I., C.-C. Wu, I.-F. Pun, and D.-S. Ko, 2008: Upper-ocean thermal structure and the western North Pacific category 5 typhoons. Part I: Ocean features and the category 5 typhoons' intensification. *Mon. Wea. Rev.*, **136,** 3288-3306.

Lin, S., W.-Z. Zhang, S.-P. Shang, and H.-S. Hong, 2017: Ocean response to typhoons in the western North Pacific: Composite results from Argo data. *Deep Sea Research Part I: Oceanographic Research Papers*, **123,** 62-74.

Manda, A., and Coauthors, 2014: Impacts of a warming marginal sea on torrential rainfall organized under the Asian summer monsoon. *Scientific reports*, **4,** 5741.

Mei, W., and C. Pasquero, 2012: Restratification of the upper ocean after the passage of a tropical cyclone: A numerical study. *J. Phys. Oceanogr.*, **42,** 1377-1401.

Moteki, Q., and A. Manda, 2013: Seasonal migration of the Baiu frontal zone over the East China Sea: Sea surface temperature effect. *SOLA*, **9,** 19-22.

Nakanishi, M., and H. Niino, 2004: An improved Mellor–Yamada level-3 model with condensation physics: Its design and verification. *Bound.-Layer Meteor.*, **112,** 1-31.

Nayak, S., and T. Takemi, 2019: Quantitative estimations of hazards resulting from Typhoon Chanthu (2016) for assessing the impact in current and future climate. *Hydrological Research Letters*, **13,** 20-27.

Price, J. F., 1981: Upper ocean response to a hurricane. *J. Phys. Oceanogr.*, **11,** 153-175.

Price, J. F., R. A. Weller, and R. Pinkel, 1986: Diurnal cycling: Observations and models of the upper ocean response to diurnal heating, cooling, and wind mixing. *J. Geophys. Res. Oceans*, **91,** 8411-8427.

Price, J. F., T. B. Sanford, and G. Z. Forristall, 1994: Forced stage response to a moving hurricane. *J. Phys. Oceanogr.*, **24,** 233-260.

Price, J. F., J. Morzel, and P. P. Niiler, 2008: Warming of SST in the cool wake of a moving hurricane. *J. Geophys. Res. Oceans*, **113**.

Reynolds, R. W., and T. M. Smith, 1994: Improved global sea surface temperature analyses using optimum interpolation. *J. Climate*, **7,** 929-948.

Reynolds, R. W., N. A. Rayner, T. M. Smith, D. C. Stokes, and W. Wang, 2002: An improved in situ and satellite SST analysis for climate. *J. Climate*, **15,** 1609-1625.

Saito, K., 2012: The JMA Nonhydrostatic model and its applications to operation and research. *InTech. Atmospheric Model Applications***,** 85-110.

Saito, K., and Coauthors, 2006: The operational JMA nonhydrostatic mesoscale model. *Mon. Wea. Rev.*, **134,** 1266-1298.

Sakai, R., and M. Yamaguchi, 2005: The WGNE intercomparison of tropical cyclone track forecasts by operational global models. *CAS/JSC WGNE Research Activities in Atmospheric and Oceanic Modeling*, **35,** 0207-0208.

Sakamoto, K., and Coauthors, 2019: Development of a 2-km resolution ocean model covering the coastal seas around Japan for operational application. *Ocean Dynamics*, **69,** 1181-1202.

Shay, L. K., 2010: Air-sea interactions in tropical cyclones. *Global Perspectives on Tropical Cyclones: From Science to Mitigation*, **4,** 93-131.

Tsuguti, H., and T. Kato, 2014: Contributing factors of the heavy rainfall event at Amami-Oshima Island, Japan, on 20 October 2010. *Journal of the Meteorological Society of Japan. Ser. II*, **92,** 163-183.

Tsujino, H., H. Nakano, K. Sakamoto, S. Urakawa, M. Hirabara, H. Ishizaki, and G. Yamanaka, 2017: Reference Manual for the Meteorological Research Institute Community Ocean Model version 4 (MRI.COMv4). *Technical Reports of the Meteorological Research Institute* **80,** 1-306.

Usui, N., S. Ishizaki, Y. Fujii, H. Tsujino, T. Yasuda, and M. Kamachi, 2006: Meteorological Research Institute multivariate ocean variational estimation (MOVE) system: Some early results. *Advances in Space Research*, **37,** 806-822.

Usui, N., and Coauthors, 2017: Four-dimensional variational ocean reanalysis: a 30-year high-resolution dataset in the western North Pacific (FORA-WNP30). *Journal of Oceanography*, **73,** 205-233.

Wu, Q., and D. Chen, 2012: Typhoon-induced variability of the oceanic surface mixed layer observed by Argo Floats in the Western North Pacific Ocean. *Atmosphere-ocean*, **50,** 4-14.

Xu, F., and A. Ignatov, 2014: In situ SST quality monitor (i Quam). *Journal of Atmospheric and Oceanic Technology*, **31,** 164-180.

Yablonsky, R. M., and I. Ginis, 2009: Limitation of one-dimensional ocean models for coupled hurricane–ocean model forecasts. *Mon. Wea. Rev.*, **137,** 4410-4419.

Yabu, S., S. Murai, and H. Kitagawa, 2005: Clear sky radiation scheme. *Separate volume of annual report of JMA-NPD*, **51,** 53-64 (in Japanese).

Zhang, H. M., R. W. Reynolds, and T. M. Smith, 2004: Bias characteristics in the AVHRR sea surface temperature. *Geophys. Res. Lett.*, **31**.